Quaternary Science Reviews 333 (2024) 108693

Contents lists available at ScienceDirect

Quaternary Science Reviews

journal homepage: www.elsevier.com/locate/quascirev

The Late Holocene deglaciation of James Ross Island, Antarctic Peninsula: OSL and ^{14}C-dated multi-proxy sedimentary record from Monolith Lake

Matěj Roman [a,b,*], Anna Píšková [c], David C.W. Sanderson [d], Alan J. Cresswell [d], Marie Bulínová [c,e], Matěj Pokorný [c], Jan Kavan [b,f], Stephen J.A. Jennings [b,g], Juan M. Lirio [h], Linda Nedbalová [c,i], Veronika Sacherová [c], Kateřina Kopalová [c,i], Neil F. Glasser [a], Daniel Nývlt [b,j]

[a] Centre for Glaciology, Department of Geography and Earth Science, Aberystwyth University, Llandinam Building, Penglais Campus, SY23 3DB, Wales, United Kingdom
[b] Polar-Geo-Lab, Department of Geography, Faculty of Science, Masaryk University, Kotlářská 2, 602 00, Brno, Czechia
[c] Department of Ecology, Faculty of Science, Charles University, Viničná 7, 128 44, Prague, Czechia
[d] Scottish Universities Environmental Research Centre (SUERC), Rankine Av, East Kilbride, G75 0QF, Glasgow, United Kingdom
[e] Department of Geosciences, Faculty of Science and Technology, The Arctic University of Norway, Tromsø, Norway
[f] Centre for Polar Ecology, Faculty of Science, University of South Bohemia, Branišovská 31a, 370 05, České Budějovice, Czechia
[g] Institute of Biochemistry and Biophysics, Polish Academy of Sciences, Pawińskiego 5A, 02–106 Warsaw, Poland
[h] Instituto Antártico Argentino, 25 de Mayo 1143, General San Martín, Buenos Aires, Argentina
[i] Department of Phycology, Institute of Botany, Czech Academy of Sciences, Dukelská 135, 379 01, Třeboň, Czechia
[j] Czech Geological Survey, Brno Branch, Leitnerova 22, 658 69, Brno, Czechia

ARTICLE INFO

Handling editor: P Rioual

Keywords:
Antarctica
Palaeolimnology
Lake sediments
Radiocarbon
OSL dating
Deglaciation
Diatoms
Faunal subfossils
Holocene
Neoglacial

ABSTRACT

Lentic waterbodies provide terrestrial sedimentary archives of palaeoenvironmental change in deglaciated areas of the Antarctic. Knowledge of the long-term evolution of Antarctic palaeoenvironments affords important context to the current marked impacts of climate change in the Polar regions. Here, we present a comprehensively dated, multi-proxy sedimentary record from Monolith Lake, a distal proglacial lake in one of the largest ice-free areas of the Antarctic Peninsula region. Of the two defined sedimentary units in the cores studied, the lower Unit 1 exhibits a homogeneous composition and unvarying proxy data profiles, suggesting rapid clastic deposition under uniform, ice-proximal conditions with a sedimentation rate of ~1 mm yr^{-1}. ^{14}C and optically stimulated luminescence (OSL) dating bracket the deposition interval to 1.5–2.5 ka BP, with the older age being more probable when compared to independent dating of the local deglaciation. The uppermost 11 cm of the record spans the last ~2.2 ka BP (maximum age), suggesting a markedly decreased sedimentation rate of ~0.05 mm yr^{-1} within Unit 2. Whereas Unit 1 shows only scarce evidence of biological activity, Unit 2 provides an uninterrupted record of diatoms (with 29 species recorded) and faunal subfossils, including the fairy shrimp *Branchinecta gaini*. Concentrations of organically-derived elements, as well as diatoms and faunal remains, are consistent, implying a gradual increase in lake productivity. These results provide an example of long-term Antarctic 'greening' (i.e. increasing organic productivity in terrestrial habitats) from a palaeolimnological perspective. The boundary between Units 1 and 2, therefore, marks the timing of local deglaciation at the final stages of a period of negative glacier mass balance, i.e. the Mid-Late Holocene Hypsithermal. Subsequent Neoglacial cooling is evidenced by the abated influence of glacial meltwater streams and turbidity decline linked to reduced glacier runoff, although most proxy responses mirror the natural proglacial lake ontogeny.

1. Introduction

Antarctic Peninsula ecosystems and geosystems are anticipated to undergo major changes over the 21st century (Lee et al., 2017; Noble et al., 2020; DeConto et al., 2021). This region is considered a sensitive component of the Earth's climate system, as evidenced by one of the

* Corresponding author.Centre for Glaciology, Department of Geography and Earth Science, Aberystwyth University, Llandinam Building, Penglais Campus, SY23 3DB, Wales, United Kingdom.
E-mail addresses: mar133@aber.ac.uk, matej.roman@mail.muni.cz (M. Roman).

https://doi.org/10.1016/j.quascirev.2024.108693
Received 7 February 2024; Received in revised form 27 April 2024; Accepted 29 April 2024
Available online 9 May 2024

most rapid observed rates of atmospheric warming globally in the second half of the 20th century (Vaughan et al., 2003) in response to ongoing climate change (Turner et al., 2016, 2020). Current impacts of climatic changes in the northeastern Antarctic Peninsula include the disintegration of ice shelves (e.g., Cook and Vaughan, 2010; Baumhoer et al., 2021), the recession of land-based glaciers (e.g., Skvarca et al., 2004; Carrivick et al., 2012; Engel et al., 2012) and increasing atmospheric temperatures (e.g., Vaughan et al., 2003; Turner et al., 2020).

In an effort to convey a longer-term perspective on Holocene climate oscillations in this region of Antarctica, a number of studies have examined natural archives in terrestrial, marine, lacustrine, and glacial settings to infer changes in past environments (e.g., Ingólfsson et al., 1998; Michalchuk et al., 2009; Mulvaney et al., 2012; Sterken et al., 2012; Palacios et al., 2020). Warmer climatic conditions were recorded in marine and terrestrial environments shortly after the retreat of the Antarctic Peninsula Ice Sheet in the Early Holocene (Ó Cofaigh et al., 2014; Nývlt et al., 2020) and later in the 'Mid-Late Holocene Hypsithermal' period (Bentley et al., 2009; Giralt et al., 2020), when local ice shelves disintegrated (e.g., Pudsey and Evans, 2001; Mulvaney et al., 2012). Receding glaciers revealed the deglaciated landscape of northern James Ross Island, suitable for the development of a high concentration of lakes (Nedbalová et al., 2013). These lakes of various types, and with diverse biotic assemblages, evolved in deglaciated areas subject to the influence of changing Holocene climatic conditions (e.g., Björck et al., 1996; Nedbalová et al., 2013; Roman et al., 2019; Kavan et al., 2021; Piccini et al., 2024). The lake basins and their ecosystems have also been affected by ontogeny, or time-dependent unidirectional processes linked to primary succession in deglaciating landscapes (Fritz and Anderson, 2013). The Mid-Late Holocene Hypsithermal was followed by cooling in the Late Holocene Neoglacial Period (Čejka et al., 2020), starting ~2 ka (thousand years) BP (= before present, 1950 CE), when local glaciers advanced (e.g., Carrivick et al., 2012; Kaplan et al., 2020; Simms et al., 2021). Warming in recent centuries accelerated during the last decades of the 20th century, principally occurring in the northern part of the Antarctic Peninsula (e.g., Vaughan et al., 2003; Mulvaney et al., 2012; Oliva et al., 2017; Turner et al., 2020; Simms et al., 2021). These environmental changes also strongly affected the Antarctic lacustrine systems and the structure of their biotic assemblages (Quayle et al., 2002; Nedbalová et al., 2017b; Píšková et al., 2019; Roman et al., 2019).

Lacustrine sediments are an excellent archive of past climatic and environmental changes (Hodgson et al., 2004; Giralt et al., 2020). Furthermore, an increasing body of evidence suggests that Antarctic lakes represent valuable terrestrial biodiversity hotspots (Laybourn-Parry and Pearce, 2007; Chown et al., 2015; Rochera and Camacho, 2019). Yet, only a comparatively small number of palaeolimnological studies have been undertaken in the northeastern Antarctic Peninsula region (e.g., Björck et al., 1996; Sterken et al., 2012; Píšková et al., 2019; Čejka et al., 2020). The first fragmentary terrestrial evidence for Holocene climatic changes in the northeastern part of the Antarctic Peninsula was presented by Rabassa (1983), Karlén et al. (1988), and Zale and Karlén (1989). In a study of 21 Antarctic lentic waterbodies, including North and South Cape Lachman lakes and Monolith Lake (the preferred name as defined in Nedbalová et al., 2013, instead of 'Boulder Lake' used in Björck et al., 1996), Hansson and Håkansson (1992) assessed the importance of environmental variables determining the species composition and abundance of periphytic diatoms. Analyses of the diatom content and chemical composition of a sediment core from a lake in the Brandy Bay area were later accomplished by Håkansson et al. (1995) to investigate the interaction between organisms, their environment, and climate. Björck et al. (1996) performed the first detailed palaeoclimatic reconstruction of the Mid-Late Holocene environmental conditions of James Ross Island (JRI), which was based on several sedimentary cores, including one from Monolith Lake. This study also featured diatom analyses, in which 43 identified (and 7 unidentified) diatom taxa were present among the three studied lakes. Yet, the authors did not specify alpha diversity for individual lakes (i.e. the richness of Monolith Lake is not given), and these analyses were performed using outdated taxonomical concepts, which assume a more cosmopolitan distribution of some taxa. Collectively, these uncertainties highlight the need for a modern reinvestigation. More recently, multi-proxy studies of lake sediments were performed on nearby Beak Island (Roberts et al., 2011; Sterken et al., 2012) and Vega Island, where Lake Esmeralda on Cape Lamb (Píšková et al., 2019) and Lake Anónima in the Devil's Bay area (Čejka et al., 2020) were investigated.

In this paper, we build upon the pioneering palaeolimnological work of Björck et al. (1996) and revisit one of the three JRI lakes that they studied, Monolith Lake. We present a high-resolution multi-proxy investigation of one of the largest lakes on the Ulu Peninsula (JRI), which complements recent studies from the adjacent Vega Island (Píšková et al., 2019; Čejka et al., 2020) and provides a more comprehensive picture of Late-Holocene environmental changes on the Antarctic Peninsula. This study is further advanced by recent progress in freshwater ecology, which has demonstrated the presence of specific autotrophic assemblages in the lakes from the region, including well-developed and specific diatom and cyanobacterial flora (Esposito et al., 2008; Komárek et al., 2008, 2012; Kopalová et al., 2011, 2012, 2013, 2019; van de Vijver et al., 2014; Hamilton et al., 2014; Zidarova et al., 2016; Bulínová et al., 2020). In their study of modern diatom communities, Kopalová et al. (2013) documented 35 taxa for Monolith Lake, yet the potential historical richness of the lake was not examined. Furthermore, recent multi-proxy studies have stressed the importance of geomorphological processes in lake catchments, as well as the impact of sudden events on deposition in Antarctic lakes (e.g., Toro et al., 2013; Roberts et al., 2017; Antoniades et al., 2018; Píšková et al., 2019). Such changes often correspond to regional climate shifts and can be traced both in lacustrine and glacial environments (Mulvaney et al., 2012; Čejka et al., 2020). Thus, this study provides not only a revised assessment of Late Holocene shifts of lake ecosystems and ontogeny, but also glimpses into processes operating on the scale of lake catchments, local glaciers, and regional climate. The resulting palaeoenvironmental context will serve as a basis for estimating the impact of ongoing climate changes on the local ecosystems and geosystems.

2. Regional context

2.1. Study area

JRI is situated in the northwestern part of the Weddell Sea, close to the northernmost tip of the Antarctic Peninsula, from which it is separated by the Prince Gustav Channel (Fig. 1). Glaciers and permanent ice cover more than 80% of the island. However, the Ulu Peninsula, located in the northern part of JRI, is one of the largest ice-free areas (~312 km^2) of the Antarctic Peninsula (Kavan et al., 2017). The bedrock of JRI is composed of two main geological units, namely i) Cretaceous to Neogene sedimentary rocks and ii) subglacial/subaqueous Neogene to Quaternary volcanic and associated sedimentary rocks (e.g., Francis et al., 2006; Nývlt et al., 2011; Smellie et al., 2013; Mlčoch et al., 2020). The majority of the igneous rock formed during glacial periods under ice cover (Smellie et al., 2008), giving rise to specific volcanic landforms, such as volcanic mesas, which attain heights of over 400 m a.s.l. (e.g. Lachman Crags, Davies Dome, Lookalike Peaks). However, some volcanic products, such as cinder and tuff cones, are of an interglacial ice-free marine origin (Nehyba and Nývlt, 2014; Calabozo et al., 2015; Smellie, 2021).

During the Last Glacial Maximum, the Antarctic Peninsula Ice Sheet coalesced with the independent Mt. Haddington Ice Cap, situated over southern JRI (Ó Cofaigh et al., 2014). After ~18 ka, the overlying ice mass became increasingly dynamic with the development of the Prince Gustav Ice Stream, leading to regional ice thinning (Roberts et al., 2011; Glasser et al., 2014), and the deglaciation of the Ulu Peninsula was underway by ~8 ka (Johnson et al., 2011; Nývlt et al., 2014). The

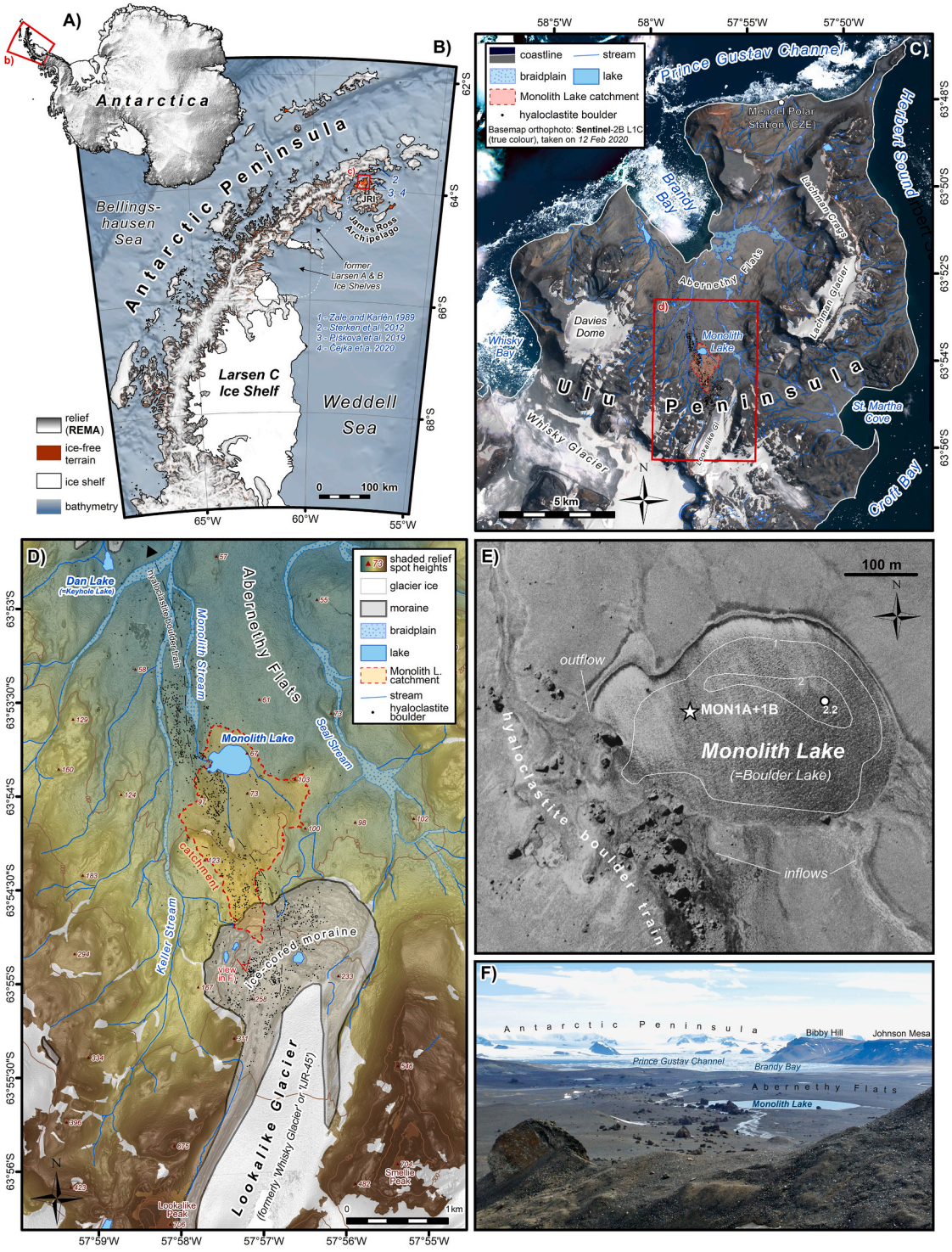

Fig. 1. Location of the study area. **A)** Position of the Antarctic Peninsula within Antarctica. Blue symbols with numbers (also in B and D) denote reference sites where palaeolimnological records have been obtained (see Table 8 for the references list). **B)** Ulu Peninsula (denoted by red frame) is located on James Ross Island (JRI), on the eastern side of the Antarctic Peninsula. The base maps are sourced from the Reference Elevation Model of Antarctica (REMA) digital elevation model (DEM) (Howat et al., 2019) and geospatial package Quantarctica 3.2 (Matsuoka et al., 2021), including BedMachine v2 Antarctica bed topography (Morlighem et al., 2020) and the SCAR Antarctic Digital Database (ADD) v7.0 shapefiles (http://www.add.scar.org/). **C)** Monolith Lake is situated in the central part of the Ulu Peninsula, one of the largest deglaciated areas in the Antarctic Peninsula region. Topographic features are from Czech Geological Survey (2009) and Jennings et al. (2021). **D)** A topographic map of the Monolith Lake catchment and adjacent area (Czech Geological Survey, 2009; Jennings et al., 2021), including Lookalike Glacier and Keyhole Lake (called 'Dan Lake' in Nedbalová et al., 2013), which was studied by Björck et al. (1996). Spot and contour elevations (in brown) are in m above sea level. Lake catchment was delineated from REMA DEM (Howat et al., 2019) and orthorectified aerial imagery, acquired by the British Antarctic Survey (Czech Geological Survey, 2009). The lake catchment area thus delineated is lesser than the previously reported value in Nedbalová et al. (2013). **E)** Aerial photograph (Czech Geological Survey, 2009) of Monolith Lake with coring site denoted; bathymetry is from Nedbalová et al. (2013) (shown as white contours and depocenter; in metres). **F)** View of Monolith Lake, looking northward from the Lookalike Glacier moraine (position shown in D by black angle), with hyaloclastite boulder train in the centre (photo credit: Michaela Kňažková).

receding glaciers revealed a deglaciated landscape with large-scale features determined by underlying bedrock geology, which had been sculpted by overlying ice masses during the preceding glacial periods (Jennings et al., 2021). Post-deglaciation modification of the ice-free terrain superimposed paraglacial and periglacial geomorphological landforms upon the remnant glacial features (Davies et al., 2013; Jennings et al., 2021). Prominent ice-cored moraines located in the proglacial areas of small cirque and valley glaciers illustrate the maximum extent attained during the most recent glacial advance (Carrivick et al., 2012).

The climate of JRI is determined by its position at the boundary between continental and maritime Antarctica. It is characterised by cold, arid barrier winds from the south, and its location in the precipitation shadow due to Antarctic Peninsula orography (van Wessem et al., 2015). Therefore, the climate is arid, with precipitation mostly in the form of snow, estimated at 300–500 mm a^{-1} (van Lipzig et al., 2004). Owing to the low humidity and often high wind speeds, evaporation and sublimation rates are high; snow is often blown out from generally flat surfaces by predominant W to SW winds (Nývlt et al., 2016; Kavan et al., 2020; Kňažková et al., 2020). The mean annual air temperature at Abernethy Flats (~2 km from Monolith Lake) was −7.3 °C between 2006 and 2016 (Hrbáček and Uxa, 2020). The mean monthly air temperature typically exceeds 0 °C during summer, and only occasionally falls below −20 °C in winter (Hrbáček and Uxa, 2020). The deglaciated areas of JRI are underlain by continuous permafrost (Obu et al., 2020).

Biogeographically, the James Ross Archipelago belongs to a transitory zone between the maritime and continental Antarctic regions (Øvstedal and Lewis-Smith, 2001; Verleyen et al., 2021). More specifically, JRI falls within the North-east Antarctic Peninsula bioregion, according to the Antarctic Conservation Biogeographic Regions (Terauds and Lee, 2016). The vegetation comprises bryophytes and lichens, located mainly in the vicinity of lakes or streams, as their distribution is usually limited by the availability of liquid water (Robinson et al., 2003; Barták et al., 2015). The micro-flora, mostly composed of cyanobacteria, green algae, and diatoms, is well-developed in freshwater ecosystems such as seepages, lakes, and streams Hawes and Brazier (1991). The construction of the Czech Antarctic J.G. Mendel Station in 2006 renewed interest in the local freshwater biota, leading to a number of studies (e.g., Komárek et al., 2008; Komárek and Komárek, 2010; Kopalová et al., 2013; Zidarova et al., 2016; Nedbalová et al., 2017a). The invertebrate fauna of lakes is dominated by crustaceans such as *Boeckella poppei* (Copepoda) and *Branchinecta gaini* (Branchiopoda) (Nedbalová et al., 2017b).

2.2. Catchment and lake description

Monolith Lake is the second largest lake on the northern Ulu Peninsula, reaching a surface area of ~0.093 km^2 and a maximum depth of ~2.2 m (Nedbalová et al., 2013). The lake is located at an altitude of 67 m a.s.l. and is classified as a stable lake in an old moraine (Nedbalová et al., 2013). The lake catchment covers an area of 1.33 km^2, as delineated from the Reference Elevation Model of Antarctica (REMA) digital elevation model (DEM) (Howat et al., 2019) and orthorectified aerial imagery, acquired by the British Antarctic Survey (Czech Geological Survey, 2009). This value differs from the catchment area of 1.89 km^2, which is based on the DEM of the Czech Geological Survey (2009) as previously reported in Nedbalová et al. (2013). There are two surficial inflows into the lake on its southern shore (Czech Geological Survey, 2009). However, most of the lake water originates from snow and active layer melt. Large boulders of hyaloclastite breccia located around the south-western shore of the lake act as effective barriers for snow accumulation (Kňažková et al., 2020) and provide an important source of meltwater during summer. Thaw from the Lookalike Glacier, also formerly referred to as IJR-45 (Rabassa et al., 1982; Davies et al., 2013), Whisky Glacier (Chinn and Dillon, 1987; Engel et al., 2012, 2018), or Massey Heights Glacier (Björck et al., 1996), and its prominent ice-cored moraine in particular, may have also contributed meltwater in the past (Fig. 1D).

Lake water temperatures exhibit a strong diurnal regime with average daily variations of 4.7 °C and an average water temperature of 4.9 °C (from 2015 to 2017 summers; Kavan, 2017; unpublished data). Monolith Lake can be considered a relatively warm and stable waterbody, with average conductivity and lower pH in comparison with other lakes on the Ulu Peninsula (a more extensive discussion on the physicochemical parameters of these lakes can be found in Nedbalová et al., 2013). Monolith Lake is usually ice-free during the austral summer (Kavan, 2017), although during the colder than usual years of 2013 and 2014 the lake remained frozen for extended periods, even during summer months (2013 and 2014 Czech Antarctic expedition members, pers. comm.). An examination of Sentinel-2 satellite imagery between 2018 and 2023 showed lake ice break-up in November–December, and freeze-up taking place between February–March. At the time of sediment coring (9:00–12:00, February 13, 2017), lake water temperature was 4.4 °C, conductivity 82 μS cm^{-1}, and pH 7.6.

Limnological surveys by Nedbalová et al. (2013, 2017b), as well as this coring campaign, confirm the continuous presence of *Branchinecta gaini* in the last 10–15 years. Observations on *B. gaini* are important given that Björck et al. (1996) claimed they had vanished from Monolith Lake after the Neoglacial cooling and have not been observed since, thereby establishing palaeoclimatic inferences. Prior to these observations, *B. gaini* was considered extinct in the North-east Antarctic Peninsula bioregion (see Discussion), and *Boeckella poppei* was not observed on this side of the Antarctic Peninsula at all (Björck et al., 1996; Gibson and Bayly, 2007).

3. Materials and methods

3.1. Sediment coring and sample preparation

Two sedimentary cores, Mon1A and Mon1B, were recovered from the west-central part of Monolith Lake (63°53′48.5″ S, 57°57′19.5″ W) (Fig. 1E). The coring was executed using an Eijkelkamp Beeker piston sampler from a rubber dinghy fixed in a stable position. The cores were transferred to the J.G. Mendel Station in a vertical position, where they were frozen, and transported frozen to Charles University, Czechia. Core Mon1A was 31 cm in length and used for the optically stimulated luminescence (OSL) and radiocarbon dating, magnetic susceptibility measurements, and faunal subfossils analysis. Core Mon1B, with a combined length of 45 cm, was composed of a 30-cm sediment core sampled in the coring chamber and 15-cm of residue embedded beneath the trigger mechanism of the sampler, and was used for abiotic and diatom analyses. Both cores were sectioned at 1 cm intervals, with core Mon1A protected from light exposure by manipulation under dim laboratory conditions.

3.2. Chronology

Accelerator mass spectrometry (AMS) ^{14}C dating was performed in Poznań Radiocarbon Laboratory (Poland) on four bulk sediment samples. Calibration of ^{14}C ages was carried out in OxCal v. 4.4 (Bronk Ramsey, 2009) using the SHCal20 atmospheric curve (Hogg et al., 2020). Radiocarbon data are reported as conventional ^{14}C years BP with 1σ error, and as calibrated years with 2σ.

Optically stimulated luminescence dating was performed at the Scottish Universities Environmental Research Centre (SUERC), East Kilbride, UK (Sanderson et al., 2017) and followed the procedures described in Píšková et al. (2019). Core Mon1A was transported to SUERC unsectioned, frozen, and carefully packed in a light-protected case. Luminescence profiling measurements were first performed on bulk sediments using the SUERC Portable OSL (pOSL) instrument (Sanderson and Murphy, 2010; Munyikwa et al., 2021), which indicated that both blue and IR stimulation yield measurable signals (Fig. A1 in

Appendix A). Laboratory-based profiling was also conducted on separated 90–250 μm grains, with infrared stimulated luminescence (IRSL) and thermoluminescence (TL) measurements undertaken on paired poly-mineral aliquots, and OSL measurements made on paired HF etched (nominally quartz) aliquots. All data were calibrated to account for sensitivity variations, and to produce equivalent dose (D_e) estimates. Differences in sensitivity between the three readout methods were observed (Fig. A2), with OSL on the nominal quartz fraction showing the lowest sensitivity, followed by IRSL and then TL on the poly-mineral fraction. The measurements showed that dose estimates vary significantly between the two units above and below 5 cm depth.

Following the pOSL and profiling measurements, OSL measurements on quartz were performed for quantitative analysis of four selected samples. The samples were processed to extract 150–250 μm quartz grains, which were dispensed to 16 stainless steel discs. These were analysed using a single aliquot regenerative (SAR) approach (Wintle and Murray, 2000) to determine the stored dose for each aliquot, with the mean estimate most closely matching the centre of the major peak of dose distribution. The weighted, unweighted, or robust mean of all the aliquots that satisfied SAR quality checks combined with the dose rate was used to determine the age of each sample (Fig. A3). Measurements were conducted using a Risø DA-15 automatic reader equipped with a $^{90}Sr/^{90}Y$ β-source for irradiation, blue LEDs emitting at ~470 nm and infrared (laser) diodes emitting at ~830 nm for optical stimulation, and a U340 detection filter pack to detect in the region 270–380 nm, while cutting out stimulating light (Bøtter-Jensen et al., 2000). Dose rates were measured using thick source beta counting (Sanderson, 1988) and high-resolution gamma spectrometry (HRGS), with the total dose rate determined from a combination of these measurements and a calculated cosmic dose rate.

The resulting age-depth model is based on Bayesian Markov Chain Monte Carlo techniques, constructed in the *Bacon* v2.5 script for R v4.2 (Blaauw and Christen, 2011; R Core Team, 2022). All SAR-OSL ages and one ^{14}C age (excluding those suffering from reservoir or hard-water effects, see section 5.1 for specific rationale and discussion) were used for the *Bacon* model. A boundary was set at the main lithological transition, with the priors for the accumulation rate *acc.mean* set at 200 and 10 a cm^{-1} above and below the boundary, respectively.

3.3. Physical and geochemical analyses

All physical and geochemical proxies were measured at a 1 cm resolution in core Mon1B. Additionally, magnetic susceptibility was also determined for Mon1A. Measurement of magnetic properties was performed on the multi-frequency Kappabridge MFK1-FA (AGICO, Brno, Czechia) at the Department of Geography, Masaryk University, Brno, Czechia. Mass-specific magnetic susceptibility (χ) was measured at frequencies of 976 (χ_{lf}) and 15 616 Hz (χ_{hf}) with an induced magnetic field of 200 mA (Roman et al., 2021).

Grain size analysis was performed using a CILAS 1064 laser granulometer at the Institute of Geology, Czech Academy of Sciences, Prague. Measurement involved 3 leaching steps: i) 15 ml 10% KOH; ii) 15 ml 35% HCl, and; iii) removing organic matter by H_2O_2, and followed the procedure thoroughly described in Píšková et al. (2019). The grain-size parameters were calculated with the Gradistat software, v8.0 (Blott and Pye, 2001), and are presented graphically (in μm) following Folk and Ward (1957).

For the determination of cation exchange capacity (CEC), a Cu-trien method was used as described in Grygar et al. (2007, 2009) and Píšková et al. (2019) by atomic absorption (Cu and Mg) and emission (Ca) spectrometry using AAS3 spectrometer (Zeiss Jena, Germany).

X-ray fluorescence (XRF) analyses were conducted at the Department of Geological Sciences, Masaryk University, Brno, on wet samples using the Delta Premium handheld analyser (Olympus Innov-X, USA) (Píšková et al., 2019). Concentrations (wt.% or ppm) of the following elements were acquired through calibration with a standard material NIST SRM 1155a: Al, Si, S, Cl, K, Ca, Ti, V, Cr, Mn, Fe, Ni, Cu, Zn, As, Rb, Sr, Zr, Pb, Th and light elements (LE, with atomic number <13, i.e. H, He, Li, Be, B, C, N, O, F, Ne, Na, Mg), as well as derived element ratios, for all Mon1B samples.

The total content of carbon (TC) and nitrogen (TN) was determined by an Elemental Analyser Flash 2000 NCS (Thermo Scientific, USA) at the Department of Soil Science, Czech University of Life Sciences, Prague. Sediment samples were homogenised to obtain a sufficient amount of the defined fine fraction (grain size of 100–200 μm). This was performed with an agate ball mill (Vibratory Micro Mill Pulverisette 0) and sieve shaker (Analysette 3 SPARTAN, Fritsch, Germany). Further measurements followed Roman et al. (2021).

The X-ray diffraction (XRD) analysis was undertaken at the Institute of Inorganic Chemistry, Czech Academy of Sciences, in Řež, Czechia. Diffraction patterns were collected with a PANalytical X'Pert PRO diffractometer equipped with a conventional X-ray tube (CuKα radiation, 40 kV, 30 mA, line focus) and a multichannel detector X'Celerator with an anti-scatter shield. Powdered samples were measured in the range of 4–100° 2Θ. More details of the measurement geometry were published in Píšková et al. (2019). Four samples were evaluated both qualitatively and quantitatively, using Rietveld method and employing the open-source programme Profex (profex-xrd.org).

3.4. Diatoms

Samples for diatom analyses were oven-dried for 24 h at 50 °C, and 1 g of dry sediment was used for sample preparation following the method described in van der Werff (1955). Specifically, sediment samples were cleaned by adding 37% H_2O_2, applying heat (80 °C) for 1 h, and the reaction completed with the addition of $KMnO_4$. After digestion and centrifugation (3 × 10 min at 3700×*g*), the material was diluted with distilled water to avoid excessive concentrations of diatom valves and to unify sample volumes. For each, 50 μl of sample was mixed with 50 μl of sonicated (10 min) microsphere solution (concentration = ~6800 MS μl^{-1}) and 400 μl of distilled water, which was then permanently mounted onto slides with Naphrax® medium. Samples and slides are stored at the Department of Ecology at Charles University, Prague, Czechia. In each sample, 400 valves were enumerated on random transects at 1000 × magnification under oil immersion using an Olympus BX43 microscope equipped with Nomarski Contrast and an Olympus DP27 camera using the cellSens Entry Imaging Software. For taxonomical identification, Zidarova et al. (2016) was used as the main source of information. In each analysed layer, quantification of microspheres enabled the calculation of diatom concentration (i.e. number of valves per gram of sediment). However, the sediment did not contain a sufficient amount of diatom valves for reliable assemblage characterisation over the entire length of the core. Therefore, core Mon1B was analysed for diatom assemblages only in the uppermost 10 cm. Diatom species counts were transformed to relative abundances (% of total diatom valves per sample), and species richness, Shannon diversity (Shannon and Weaver, 1949), and evenness (Pielou, 1966) were calculated.

3.5. Faunal subfossils

Samples for subfossil analysis were oven-dried at 50 °C for 8 h. Subsequently, 1 g of dry sediment was transferred into 50 ml of 10% KOH, heated to 95 °C, and stirred on a magnetic plate for 30 min to deflocculate the sediment and dissolve organic acids (Szeroczyfiska and Sarmaja-Korjonen, 2007). The digested sample was then washed with tap water through a 40 μm phosphor bronze screen to remove the smaller fraction and dissolved substances. The remaining material on the screen was transferred to a flat-bottom flask, filled with water to bring the total volume to 50 ml, and stained with few drops of safranin. Successively, 1/10 of the total volume was viewed under a Nikon Eclipse 300 microscope, and all animal-derived subfossils were counted, and if

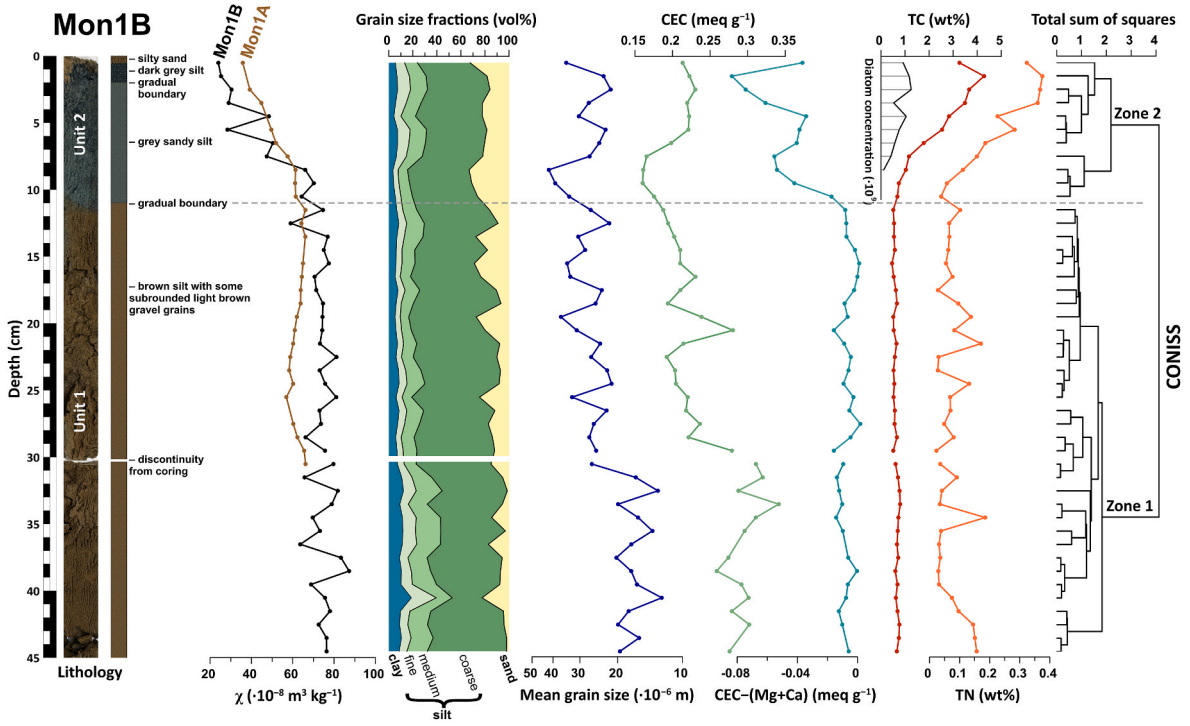

Fig. 2. Lithological profile description and physical-chemical proxies of Mon1B: low-frequency magnetic susceptibility (χ; also shown for Mon1A), volumetric percentage share of grain size fractions, mean grain size (note that the x-axis is reversed and logarithmic, for the sake of easier comparisons with grain size fractions and CEC), cation exchange capacity (CEC) and CEC−(Mg + Ca), total carbon (TC) and nitrogen (TN) content, and C/N ratio. CONISS dendrogram based on abiotic proxies separates (dashed line) the record into two main zones, complying with the lithologically distinguished units. Diatom concentration (in 10^6 valves g^{-1} of dry sediment, with values shown on the x-axis of TC) is displayed to allow for comparison with TC and other proxies.

possible, identified. Subfossils were counted as the number of remains per gram of dry weight. The uppermost 12 cm of the Mon1A core were analysed continuously. Below this depth, only every third section was examined, as the lower part of the core presented an organic-poor zone (Fig. 2).

3.6. Statistical analyses

Zonation was determined using a stratigraphically constrained incremental sum of squares cluster analysis (CONISS) on abiotic proxy data (χ_{lf}, grain size, TC, TN, XRF (excluding LE) and CEC) in the R package 'rioja' (Juggins, 2017). A principal component analysis (PCA) of standardised physical and geochemical proxies (20 variables in total) was performed in Statistica (TIBCO Software Inc., 2018, v. 13). The two principal components with the highest eigenvalues (PC1 and PC2) were extracted. Calculation of correlation coefficients and their visualisation was performed using the R package 'corrplot' (Wei and Simko, 2016; R Core Team, 2022). Missing values, or values beyond the detection limit, were excluded from numerical analyses or replaced by the mean in the case of factor analysis. All presented correlations are significant at the $\alpha = 0.01$ level unless stated otherwise.

4. Results

Both sedimentary cores consist of two clearly distinguishable units; homogeneous brown silt below the slightly gradual boundary at 11 cm depth (Unit 1), and homogeneous grey sandy silt above (Unit 2) (Fig. 2). In the upper 2 cm of core Mon1B, dark grey silt and brown silty sand layers were observed. A detailed core description and photograph are available only for core Mon1B, since Mon1A was cut in the dark room lab to prevent exposure to light.

4.1. Geochronology

Results of radiocarbon and SAR-OSL dating are shown in Tables 1 and 2, respectively. No organic remains suitable for ^{14}C dating were macroscopically identified throughout the cores. Radiocarbon ages on bulk sediment revealed one Late Holocene age and three ages from the Last Glacial Maximum period (generally defined as 18–26 ka BP). The sample MON1A_8 exhibits a practically identical age (1555 ± 90 cal. a BP) as the three ages from the sedimentologically corresponding Units 3 and 4 (albeit at lower depth) of the Monolith Lake sequence reported by Björck et al. (1996). The pOSL net signal displays an exponential trend with depth in the upper 11 cm before plateauing, with values increasing again below 25 cm. Luminescence profiling revealed ages <0.7 ka in the top 5 cm. However, samples below this depth show no clear trend and oscillate around 1.5–3 ka. SAR-OSL ages follow this pattern, revealing an age of ~0.4 ka in Unit 2, whereas two samples in Unit 1 reach ~2.4 ka. The resulting age-depth model (Fig. 3) suggests that Unit 1 was deposited between 2.5 and 2.2 ka, followed by slower accumulation in the last 2.2 ka. The sedimentation rate of ~1 mm yr^{-1} in Unit 1 decreases to ~0.05 mm yr^{-1} on average in Unit 2. The OSL-based accumulation trend in Unit 1 is consistent even when the curve is aligned (i.e. offset parallel towards younger age) through the radiocarbon ages of MON1A_8 and the three ages from Björck et al. (1996).

4.2. Physical proxy data

The profiles of χ are similar for both cores studied. Below 8–10 cm, χ reaches values 60–90·10^{-8} m^3 kg^{-1}, whilst towards the tops of the cores χ drops to 20–40·10^{-8} m^3 kg^{-1}. Only χ_{lf} is displayed in Fig. 2, as both χ_{lf} and χ_{hf} exhibit an almost identical profile, with χ_{hf} values lower by a few percent.

Mon1B sediment is comprised of poorly sorted coarse to sandy silt. Particle size distribution is mostly unimodal, although bimodal to

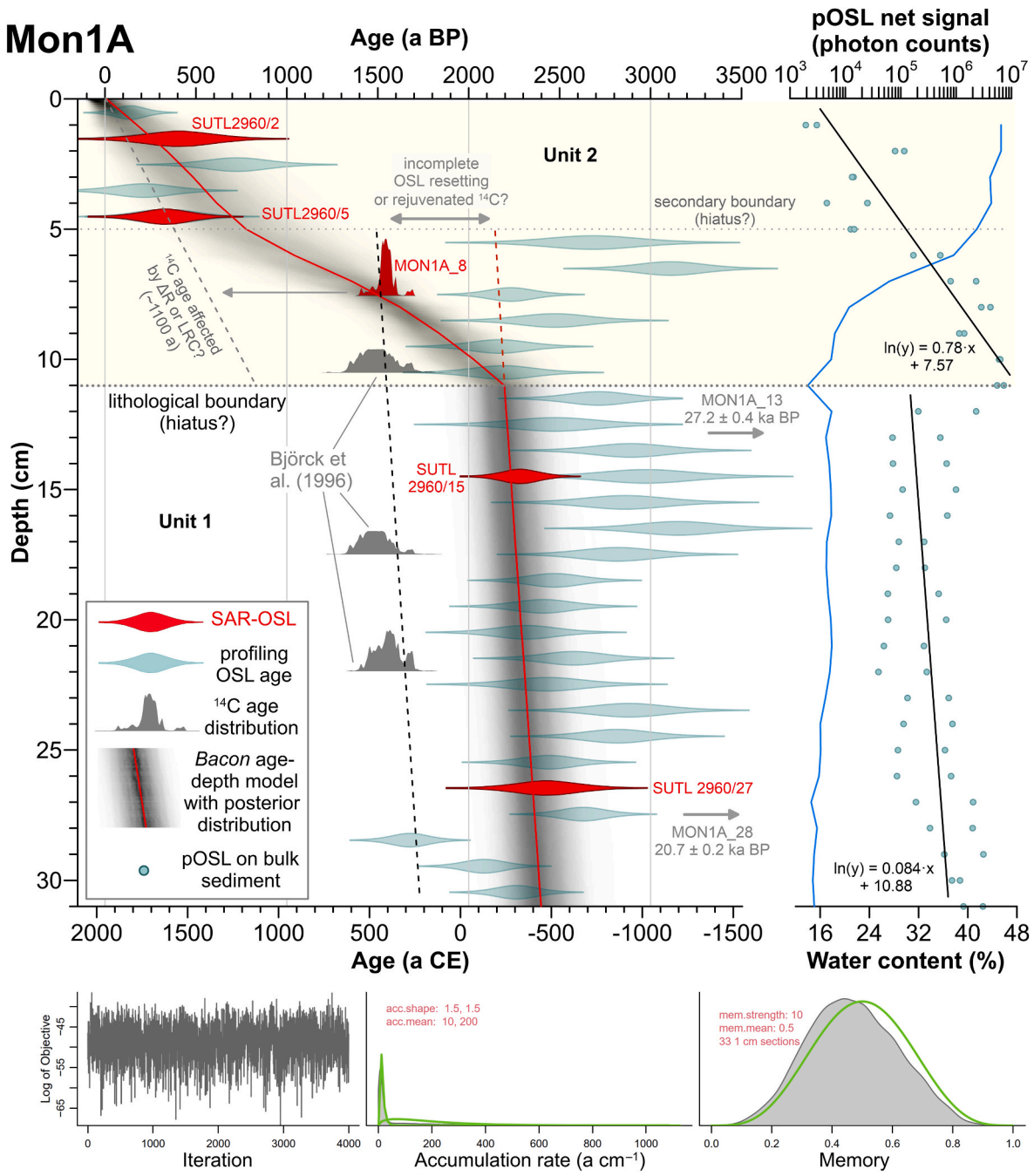

Fig. 3. Bayesian age-depth model produced in *Bacon* was based on four SAR-OSL and one accepted ^{14}C ages, with a boundary set at the lithological unconformity at 11 cm. Red line denotes the best-fit median age. Dashed red line represents an alternative age-depth model for the depth 5–11 cm, based on SAR-OSL and profiling OSL ages, and omitting the ^{14}C date MON1_8. A parallel offset of this model, the accumulation rates being identical, towards the younger ^{14}C ages in 5–31 cm depth (including the ages of Björck et al., 1996) is denoted by a black dashed line. All ages (luminescence and radiocarbon) are expressed with 2σ error. Profiling OSL ages have been combined with a consideration of the dose rate date derived from the 4 SAR dating analyses. pOSL net signal on logarithmic scale and water content (blue line) measured on bulk sediment are shown to the right. The set-up and run parameters for the primary *Bacon* age-depth model are presented in the lower panels.

trimodal modes are found more often in the lowermost 15 cm of the core. Core Mon1B is dominated by a coarse silt fraction (Fig. 2). The clay fraction shows only minor variability within the core, with the samples exceeding 10 vol% below 31 cm. On the other hand, the sand fraction increases towards the top, with several samples exceeding 30 vol%. This is reflected in the overall coarsening of the sediment from bottom to top, with mean grain size (MGS) generally increasing from ~10 to ~40 μm.

4.3. Geochemical composition

The variations of organic-derived elements – TC and TN – which were determined in core Mon1B, are presented in Fig. 2. TC and TN reach very low values of less than 1% and 0.2%, respectively, below 10 cm. The top 10 cm sees a gradual increase of both proxies to the maxima of ~4.3% and ~0.38% at 2 cm depth. TN displays higher variability, perhaps as a result of very low values near the detection limit. This is reflected in a variable C/N ratio profile, with values widely ranging from ~4 to ~23. In the top 10 cm, the C/N ratio stabilises at a mean value of

Table 1
Radiocarbon ages from Monolith Lake calibrated to calendar years before present (BP, relative to 1950 CE) using SHCal20 calibration curve (Hogg et al., 2020). Ages from Björck et al. (1996) were also recalibrated according to the latest ^{14}C calibration curve. TOC = total organic carbon.

Sample	Lab ID	Depth (cm)	^{14}C age (a BP ± 1σ)	Mean age (cal. a BP ± 2σ)	Min.–max. age (cal. a BP ± 2σ)	Note
This study						
Mon1A_8	Poz-106459	7.5	1695 ± 30	1555 ± 90	1430–1695	bulk, >1 mg C
Mon1A_13	Poz-106664	12.5	22 930 ± 170	27 200 ± 400	26 500–27 650	bulk, 0.3 mg C
Mon1A_28	Poz-106665	27.5	17 200 ± 100	20 710 ± 235	20 495–20 925	bulk, 0.5 mg C
Mon1B_43	Poz-106666	42.5	21 250 ± 140	25 535 ± 330	25 230–25 835	bulk, >1 mg C
Björck et al. (1996)						
Boulder L 8-13	Lu-3095	8–13	1630 ± 100	1520 ± 210	1310–1715	bulk, 3.2% TOC
Boulder L 15-20	Lu-3094	15–20	1620 ± 80	1505 ± 180	1350–1700	bulk, 4.4% TOC
Boulder L 20-24	Lu-3124	20–24	1690 ± 60	1580 ± 155	1415–1710	bulk, 3.6% TOC

Table 2
Summarised results of effective dose rates and SAR-OSL measurements, including calculated mean apparent ages, from sedimentary core Mon1A samples.

SUTL Lab No.	Depth (cm)	Water content[a] (%)	Equivalent Concentration[b]			Effective dose rate (mGy yr-1)			SAR-OSL			
			K/%	U/ppm	Th/ppm	Beta[c]	Gamma[d]	Total[e]	No. of discs	Recycle ratio	De (Gy)	Apparent age[f]
2960/2	1.5	50 ± 5	1.73 ± 0.27	3.07 ± 0.4	10.6 ± 1.1	1.10 ± 0.06	0.85 ± 0.04	2.12 ± 0.07	6	1.068 ± 0.077	1.01 ± 0.35	0.48 ± 0.17
2960/5	4.5	50 ± 5	1.70 ± 0.23	3.00 ± 0.34	11.0 ± 0.9	1.18 ± 0.06	0.85 ± 0.04	2.19 ± 0.08	7	1.114 ± 0.079	0.88 ± 0.25	0.40 ± 0.12
2960/15	14.5	20 ± 5	2.00 ± 0.21	2.79 ± 0.3	12.3 ± 0.7	1.93 ± 0.11	1.20 ± 0.06	3.30 ± 0.13	11	0.907 ± 0.034	7.60 ± 0.05	2.30 ± 0.09
2960/27	26.5	20 ± 5	2.20 ± 0.21	3.3 ± 0.31	11.6 ± 0.7	1.92 ± 0.11	1.20 ± 0.06	3.29 ± 0.12	10	0.979 ± 0.034	8.03 ± 0.38	2.44 ± 0.15

[a] Assumed *in situ* percentage water content is based on an estimate mean of the measured field and saturated water content of samples shortly after opening the core.
[b] Determined by HRGS (Conversion factors based on NEA (2000) decay constants): ^{40}K: 309.3 Bq kg^{-1} % K^{-1}, ^{238}U: 12.35 Bq kg^{-1} ppm U^{-1}, ^{232}Th: 4.057 Bq kg^{-1} ppm Th^{-1}.
[c] Effective beta dose rate combining water content corrections with inverse grain size attenuation factors obtained by weighting the 150–250 μm attenuation factors of Mejdahl (1979) for K, U.
[d] Mean of sample and neighbouring samples from HRGS with water content corrections.
[e] Includes a cosmic dose contribution.
[f] Rounded to the nearest decade.

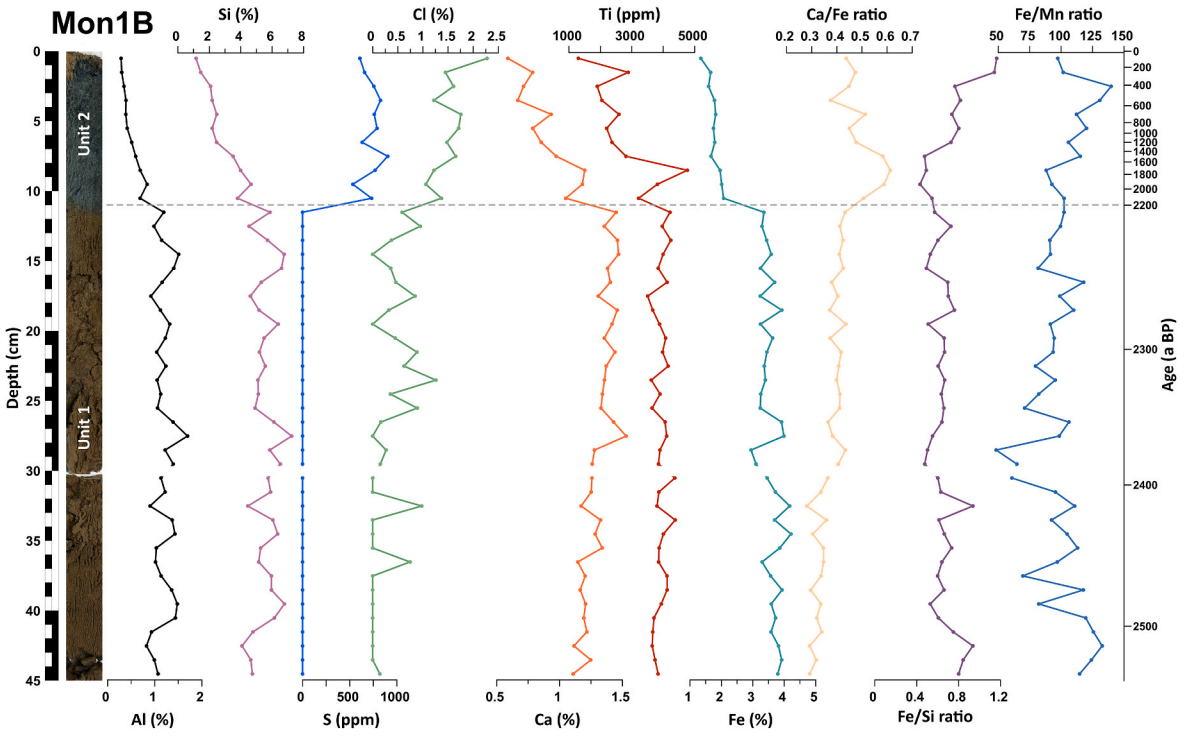

Fig. 4. Down-core variations of geochemical proxy data in Mon1B: the content of Al, Si, S, Cl, Ca, Ti, Fe, and element ratios Ca/Fe, Fe/Si and Fe/Mn. The best-fit median age-depth model is shown on the right y-axis (the age of the lowermost 15 cm was extrapolated beyond the oldest OSL date in Mon1A, however, the difference equals to less than ~150 years).

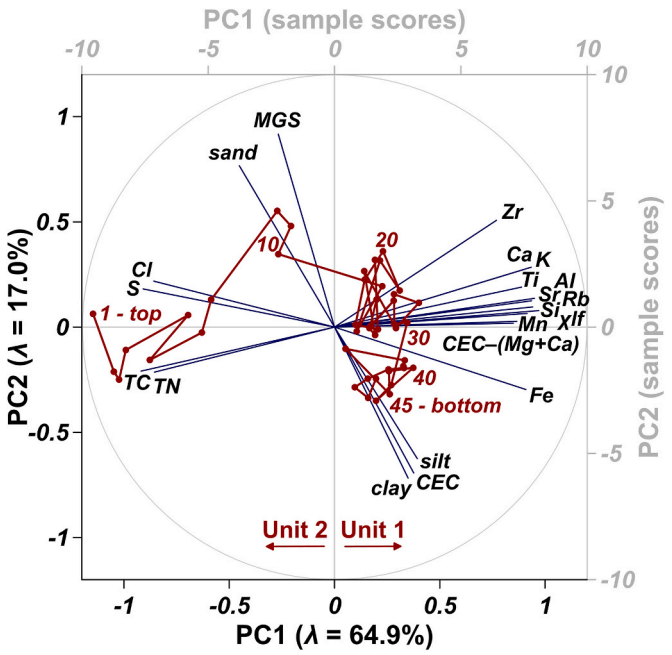

Fig. 5. Principal components analysis (PCA) of selected physical and geochemical proxies in core Mon1B explains 81.9% of overall variance in the abiotic dataset. Sample scores are plotted by red dots, with a line (numbers corresponding to depth) depicting the pathway of PC values from bottom to top of the core.

~10.

CEC and CEC−(Mg + Ca) profiles are shown in Fig. 2. Both proxies show a decreasing trend from bottom to top. CEC values range from 0.35 to 0.15 meq g^{-1}. CEC−(Mg + Ca) reaches values from −0.08 to 0. CEC is correlated most closely with the clay fraction ($r = 0.65$), whereas CEC−(Mg + Ca) shows a similar trend as χ. The two main zones (1 and 2) identified by CONISS from abiotic proxy data (in the absence of diatoms or other biological data throughout the core) correspond to the lithologically distinguished Units 1 and 2, respectively.

XRF-derived concentrations show (Fig. 4.) Si, Fe, Ca, Al, K, and Cl are the most prevalent elements detected in Mon1B beside the unspecified light elements (LE; atomic number $Z < 13$). Correlations among selected elements (and other physical proxies; Fig. A4) for Mon1B show the following element associations: Al + Si ($r = 0.98$), Zn + As + Fe ($r > 0.91$), Rb + Sr + K + Cu ($r > 0.91$), Ca + K + Ti ($r = 0.87$) and S + Cl ($r = 0.8$). While the former four groups of elements show strong positive correlations among each other, as well as with Mn, Ni, Zr, and Pb, the latter grouping of elements is correlated only with Cd and LE. The PCA (Fig. 5) displays the main source of variability in the sedimentary record. PC1 distinguishes between lithogenic elements, χ and CEC−(Mg + Ca) on one side and organically-derived elements (TC, TN), S and Cl on the other side. Overall, PC1 explains 64.9% of the variability. All lithogenic elements determined from XRF correlate with each other forming one group, only Fe and Zr differ slightly along the PC2 axis. PC2 (λ = 19.4%) is mainly influenced by grain size changes. CEC, silt, and clay fractions are positively correlated with PC2, whereas the sand fraction, MGS, and element ratios Ca/Fe, Zr/Ti, and Zr/Rb correlate negatively.

4.4. Mineral composition

The Mon1B sediment primarily consists of quartz, smectite, and feldspars (microcline and albite). Accessories minerals are mica (illite), clinoptilolite, hornblende, kaolinite, gypsum, and vermiculite or chlorite. The mineral composition shows small variability along the core; however, we observe that the quantity of quartz increases toward the top of the core, whereas the quantity of smectite decreases. The highest proportion of the crystalline material (25–37%) is composed of quartz, followed by smectites, or more likely interlayered illite/smectite (22–34%), and finally feldspars: albite (15–20%) and microcline (7–13%). The remaining proportion is distributed among other accessory minerals: illite (3–5%), chlorite (3–7%), kaolinite (2–3%), and others.

4.5. Diatom species abundance and composition

Diatom assemblages analyses in the upper 9 cm of the Mon1B core resulted in a total of 3600 counted valves and a flora of 29 species representing 20 genera (Fig. 6). Below this depth, insufficient numbers of valves were found for assemblage analyses, especially in Unit 1, where diatoms were observed only sporadically. The number of species varied between 13 and 25, with an average of 18 species per sample. The most species-rich genera were *Planothidium* with 4 species, followed by *Psammothidium* and *Stauroneis* with 3 species, each. However, the most abundant species was *Staurosirella frigida*, representing 21.4% of all counted valves, followed by *Nitzschia kleinteichiana* (21.2%) and *Nitzschia annewillemsiana* (17.9%). Diatom concentration increases upwards from the lowest values in Unit 1, to the maximum observed valve abundance, which exceeded 1×10^9 g^{-1}, at 2–3 cm depth. Species richness values were greatest at 1–2 cm with 25 species, and decreased with depth, reaching only 13 species in the lowest counted layer (8–9 cm). Shannon diversity values fluctuated between 2.49 and 1.78, with an average value of 2.14. Evenness values ranged from 0.58 to 0.77, with an average of 0.74.

4.6. Faunal subfossils

Subfossils were analysed in 18 out of 30 cm sections of the Mon1A core (Fig. 7). The uppermost 12 cm were examined continuously. The peak in abundance of the most common remains occurred at 1–2 cm depth and was followed by a rather gradual decrease to 11–12 cm, where no faunal subfossil remains were found. Below this depth, only every third section was examined (6 in total). In total, 15 different types of remains were counted in the sedimentary profile – cysts of fairy shrimp *Branchinecta gaini*, endo/exopodite setae of *B. gaini*, eggs of calanoid copepod *Boeckella poppei*, loricae of the rotifer *Notholca* sp., and six different types of tardigrade eggs, four of which were identified according to Gibson and Zale (2006), Gibson et al. (2007) and Cromer et al. (2008) as *Dactylobiotus* cf. *ambiguus*, *Acutuncus antarcticus*, *Mesobiotus (=Macrobiotus) furciger,* and *Mesobiotus (=Macrobiotus)* cf. *blocki*. Lastly, five different types of unidentified propagules of possible faunal origin (LM1–LM5) were counted. See Appendix B for a more detailed description of quantified subfossil remains. In addition to that mentioned above, several different subfossil objects were encountered, although not quantified. The most abundant were thecae of different *Difflugia* species (Arcellinida, Amoebozoa), which were found in the upper 11 cm of the core.

Remains of *B. gaini* were encountered in the uppermost 11 cm. Precise quantification of cysts was hindered by various states of their disintegration, with no clear trend with depth observed in this regard. Endo/exopodite setae were typically found freely, seldom attached in higher numbers (max. of 6) to a remnant of a limb. In addition to these appendages, endite setae were also encountered (0–9 cm), but not quantified, as they comprised “combs” of different lengths. Eggs of *B. poppei* were rare; their record was discontinuous (absent at 2–3 and 4–5 cm) and ended entirely at 8–9 cm. The most common remains were eggs of the freshwater tardigrade *Dactylobiotus* cf. *ambiguus* (up to 6000 eggs g^{-1}), which were also the only type of remains found multiple times, although sporadically, below 11 cm (Fig. 7). Eggs of other species were much rarer; in total, six eggs of limno-terrestrial species *Acutuncus antarcticus* and one egg of both *Mesobiotus furciger* and *Mesobiotus blocki*, which are primarily terrestrial, were observed. As the latter was previously only found in continental Antarctica, the nomenclature *Mesobiotus*

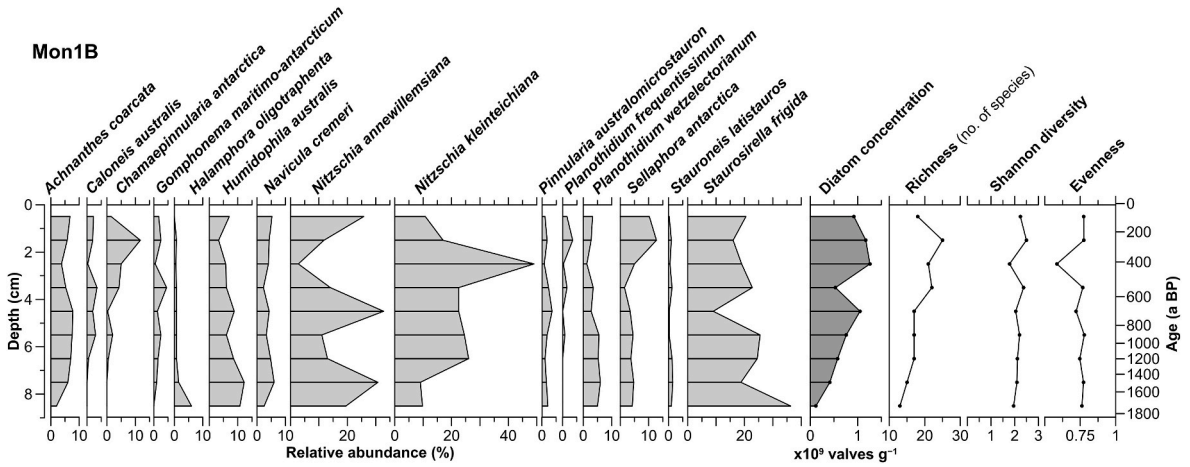

Fig. 6. Diatom stratigraphy of the top 9 cm of Mon1B core (most of Unit 2) showing the detected species with the overall relative abundance >1% throughout the core, and calculated indices: diatom concentration, richness, Shannon diversity, and evenness. The four analysed layers in Unit 1 are not shown as the diatom concentration ranged from 1.5×10^{-1} to 2.4×10^{4} g^{-1}, i.e. several orders of magnitude lower than in Unit 2.

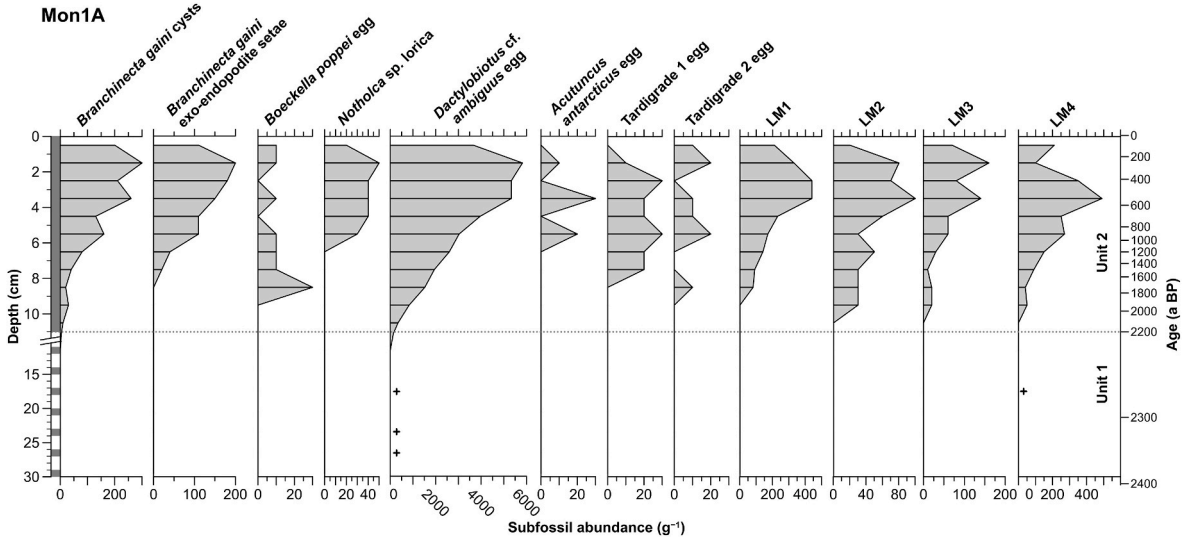

Fig. 7. Faunal subfossil stratigraphy of core Mon1A. The analysed layers are depicted in the left by grey shading. The plus signs denote the rare occurrence of subfossil remains in Unit 1 (see Appendix B). LM1–LM4: unidentified propagules of possible faunal origin.

'cf.' *blocki* is thus preferred. Two more ornamented types of tardigrade eggs were present in the sediment but not identified (see Appendix B). Records of the rotifer *Notholca* sp. ended at 5–6 cm depth.

5. Discussion

5.1. Geochronological and abiotic proxy data evidence of deglaciation in Monolith Lake sediment

Three out of four radiocarbon dates from the Monolith Lake sedimentary sequence returned ages between 20 and 28 cal. ka BP (i.e. the peak Last Glacial = Pleniglacial conditions), when the entire Antarctic Peninsula (except nunataks) was covered by a thick ice sheet (Ó Cofaigh et al., 2014; Nývlt et al., 2020), preventing lacustrine sedimentation. These high bulk-sediment ages from Unit 1 seem to be affected by old ^{14}C-depleted carbon derived from carbonate-rich Cretaceous bedrock (e.g. kerogen; Brachfeld et al., 2003), the reservoir effect (Bird et al., 1991), or allochthonous glacial/permafrost sources (Björck et al., 1991; Gore, 1997; Verleyen et al., 2004; Píšková et al., 2019), and have been excluded from the age-depth model. The absence of dateable terrestrial or (at least) aqueous macrofossils in Antarctic lakes is a recognised obstacle for establishing reliable and high-precision chronologies (Björck et al., 1991; Hjort et al., 1997; Hendy and Hall, 2006). Bulk sediment samples generally have greater reliability at higher values of TOC or C/N ratio, as the increased proportion of organic C is less prone to contamination by ^{14}C-depleted bedrock carbonates or hardwater-affected carbon (Strunk et al., 2020). The ages of ~1.5 cal ka BP in the relatively organic-rich layers of core Mon1A (8 cm depth), as well as the Monolith Lake core of Björck et al. (1996) (8–24 cm depth), are therefore considered closer to the true age of the sediment, especially since they are isochronous (within 2σ error). All these dates may have still been similarly affected, but to a lesser degree than the three excluded ^{14}C ages from our core, returning LGM ages, which come from the organic-poor Unit 1. Björck et al. (1996) dated only the organic-rich layers (equivalent to our Unit 2), where the amount of ^{14}C reservoir or influence by ^{14}C-depleted carbon is uncertain (the same applies for our ^{14}C age Mon1A–8), but certainly lower than our apparent LGM ages.

The new OSL ages point to an event of rapid sedimentation at ~2.5–2.2 ka BP, followed by a gradual accumulation of the topmost, increasingly organic-rich sediments within the last 2.2 ka BP. The pOSL and luminescence profiling in particular suggest rapid accumulation below 11 cm depth, which is supported by the combined absolute SAR-

OSL and ^{14}C ages, and very homogeneous lithostratigraphy of Unit 1, consistent with mixing. The sediment below 11 cm is rich in clastic material, as evidenced by high χ (Fig. 2) and lithogenic element proportions, but low in its content of organically-derived elements (Figs. 4 and 6) and subfossils (Figs. 6 and 7). The boundary between Units 1 and 2 at 11 cm thus signifies a sudden change of environmental conditions, and perhaps represents a short hiatus or diastem (minor sedimentary break), as noted already by Björck et al. (1996). OSL dating can furthermore help resolve the discrepancy between our and Björck et al.'s (1996) topmost parts of the sedimentary sequence. In the pioneering work of Björck et al. (1996), the most organic-rich layer is overlain by more minerogenic sediment near the top, whereby the onset of the Neoglacial conditions and vanishing of fairy shrimp *B. gaini* from JRI were inferred. However, this uppermost layer was not directly dated due to insufficient carbon content (Björck et al., 1996). In our cores, we do not observe the return of minerogenic sedimentation nor the absence of *B. gaini* (Figs. 2, 4 and 8), but infer that continuous sedimentation has occurred in the last ~2.2 ka. Neither was the presence of tephra detected in our study, either visually or by magnetic or geochemical proxy data (Roberts et al., 2011; Sterken et al., 2012; Mulvaney et al., 2012). This is inconsistent with findings of Björck et al. (1996), who inferred a tephra horizon at 5.5–8 cm depth from increased high induced remanent magnetisation (HIRM) and S-ratio.

The contrast between our sedimentary sequence and the core profiles from Björck et al. (1996) may arise from differences in the coring location within Monolith Lake, as lateral facies may change due to the action of the two inflowing streams or slumping, which could have influenced the distribution of sediment within the lake basin. Alternatively, the discrepancy could be due to the use of different coring equipment; in our case a piston corer, whilst Björck et al. (1996) employed a Russian chamber corer. While the latter prevents vertical compaction (especially near the top), the coring chamber is also not efficiently sealed, and the need to open the corer horizontally is unfavourable for obtaining the uppermost, often soft sediments with high water content (Glew et al., 2002). Björck et al. (1996) indeed acknowledged this shortcoming, and noted the possibility of loss or mixing of the topmost sandy-silty layer, which raises questions on the intactness of their sedimentary sequence. After much consideration, we propose that our boundary at 11 cm depth equates with Björck et al.'s transition at 26 cm depth, where both sedimentary records exhibit a transition from clastic to more organic sedimentation. ^{14}C ages in our Unit 1 then equate Björck et al.'s Units 3 and 4. The differences are then that Björck et al.'s Units 3 and 4 cover 19.5 cm, whereas our Unit 1 is only 11 cm thick, followed by a shift to more clastic sedimentation in the upper 6.5 cm of Björck et al.'s core – which has been attributed to the aforementioned loss, or rather mixing, of the core's top (Björck et al., 1996).

The two sedimentary units in our sequence are interpreted to capture lake ontogeny from a terminoglacial lake accumulating mixed age sediments from glacier runoff, transitioning after ~2.2 ka BP to an ice-distal proglacial lake where accumulation rate decreases and autochthonous organic carbon is present (e.g., Rouillard et al., 2012; Balascio et al., 2013). Unit 1 consists of glacial outwash, possibly when the lake was in direct contact with the glacier or in an ice-proximal glacier foreland. Most OSL and radiocarbon ages overlap (within error) in Unit 1, which is consistent with well-mixed material. The transition between Unit 1 and 2 possibly marks the juncture at which the lake is distal enough from the glacier for the turbidity to decline (at least seasonally or under lake-ice cover) to the point that biological communities are able to establish (increased TC, TN, and diatom concentration as a proxy for productivity; Webster et al., 1996). At this point, the ^{14}C ages generally become younger up-core, which is likely a product of autochthonous production dominating over allochthonous/mixed carbon sources. The upward coarsening trend may also reflect a diminishing input of glacial silt (as most glacier meltwater has probably been re-routed from Monolith Lake inflows to Seal and Keller streams system; Kavan et al., 2017) and,

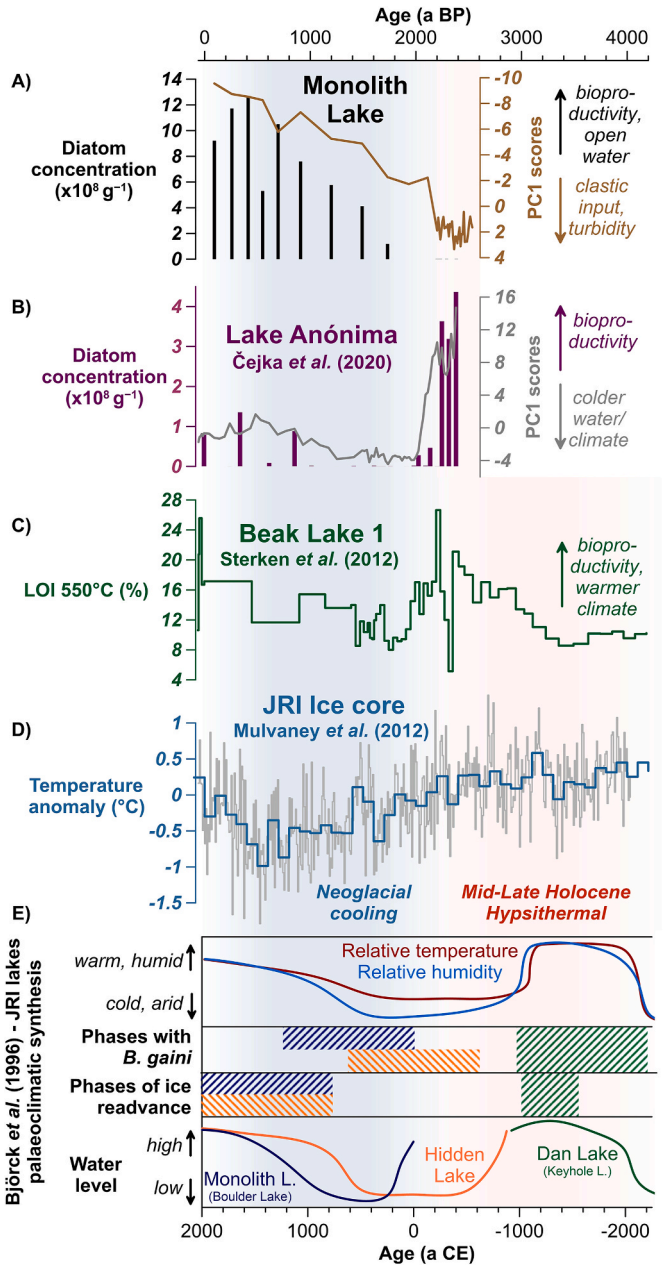

Fig. 8. Synthesis of Late-Holocene palaeoclimatic records from Eastern Antarctic Peninsula region. **A)** Diatom concentration and PC1 scores (positive values signify increased clastic input; note the reversed y-axis) in cores Mon1A and Mon1B from Monolith Lake. **B)** Diatom concentration and PC1 scores (positive values signify increased deposition of organic material and bioproductivity, ergo warmer climate) in a sedimentary core from Lake Anónima on Vega Island (Čejka et al., 2020). **C)** Loss-on-ignition (LOI 550 °C) as a proxy for organic content and hence warming in Beak Lake 1 record (Sterken et al., 2012). **D)** Reconstructed air temperature anomaly on James Ross Island from Mount Haddington ice core (black line denotes 100-yr average, grey line represents 10-yr average) (Mulvaney et al., 2012), with pan-Antarctic millennial-scale climatic excursions denoted. **E)** Synthesis of palaeolimnological records from James Ross Island by Björck et al. (1996), including the sedimentary sequence from Monolith Lake (dark blue). Note that the age-depth models of these reconstructions are based on uncalibrated ^{14}C ages and have not been updated due to lack of information on construction of these chronologies (See Table 1 for calibration of Monolith Lake ^{14}C ages from Björck et al., 1996).

conversely, a greater influence of aeolian sand (Rydberg et al., 2016; Kňažková et al., 2020). Unit 2 then captures the separation from glacial meltwater sources and the natural postglacial colonisation and succession of lacustrine microflora and invertebrates (see below).

Furthermore, independent evidence for Monolith Lake deglaciation is provided by ^{36}Cl exposure dating of a hyaloclastite boulder train in the vicinity of Monolith Lake (Jennings et al., unpublished data), which constrains the local deglaciation to ~4–2.7 ka. The palaeoenvironmental inference, therefore, posits the retreat and down-wasting of the Lookalike Glacier, or a flow unit (cf. Jennings and Hambrey, 2021) of a larger glacier body within the Brandy Bay amphitheatre (Davies et al., 2014), prompted the formation of Monolith Lake at ~2.5 ka, whereby the majority of sediment deposited in a short period of accelerated melting and sediment mobilisation. Björck et al. (1996) also interpret the lowermost Monolith Lake sediments as signalling the deglaciation. The hyaloclastite boulder train, left behind by the receding Lookalike Glacier and extending from its current ice-cored moraine complex towards Brandy Bay (Jennings et al., 2021; Jennings et al., unpublished data), may have acted as a shallow sill that dammed glacier meltwaters (Nedbalová et al., 2013). Owing to the presumed dominant down-wasting of the Lookalike Glacier, the OSL-dated material was probably transported over only a short distance from its source. In the Polar regions, where the solar resetting is commonly inadequate (Hodgson et al., 2009; Levy et al., 2017), a certain residual dose is to be expected. It is probable that the deposition age of the lower sedimentary layers of Monolith Lake is bracketed by the younger ^{14}C and older SAR-OSL ages to ~1.5–2.5 ka BP. However, in view of the other independent information given above, we posit that the local deglaciation falls within the interval of ~2.5–2.2 ka.

5.2. Subfossil stratigraphy interpretation

Two biozones were defined based on the distribution of diatom and faunal subfossil remains (Fig. 7): the organic-poor zone below 11 cm (corresponding to Unit 1), and the organic-rich zone of the upper 11 cm (Unit 2). This division was congruent with abiotic proxies. Unit 1 was nearly free of any biota. This zone represents a rather brief period of lake formation associated with high sedimentation rates. Therefore, it is possible that higher material input to the lake during this period maintained turbidity at levels that limited benthic primary production, which typically supports the whole food web in Antarctic lakes (Gibson et al., 2006). Thus, Monolith Lake could have been too unproductive to leave any trace of biological remains in the sediment. Conversely, Unit 2 was characterised by the presence of various freshwater invertebrates (and thecate amoebas). Abundances of subfossil remains in Unit 2 mirror TC and χ curves (Fig. 2). A steady increase of numbers beginning immediately after the transition between zones (i.e. ~2.2 ka BP) was followed by a slight decline in the most recent period (~0.2 ka BP). Therefore, recent climate change associated with higher water temperatures, and manifested in Maritime Antarctica by an increase in lake productivity (Quayle et al., 2003), was not unambiguously observed in faunal subfossils. However, this signal could be obscured by natural lake ontogeny or coarser sediment sectioning, since the most recent segment covers the last 200 years, and the overall trend of increasing bioproductivity is consistent with the extensive shifts of the Antarctic terrestrial ecosystems (Amesbury et al., 2017).

In this study, we characterised diatom assemblages continuously only for the top ~10 cm of sediments, due to a pronounced decrease in valve abundance at lower depths. Although diatoms were still occasionally observed at lower depths in our analyses, they were not found in sufficient numbers for robust assemblage characterisation. While the average number of valves within the top 10 cm was ~7×10^8 valves per gram of dry sediment, the lower layers did not exceed 1×10^4 valves g^{-1}. Due to the high concentration of fine sediments, coupled with low diatom valve concentrations, this made quantitative enumeration of diatom valves logistically unfeasible, regardless of the amount of input sediment. While Björck et al. (1996) reported diatom assemblage data for the whole length of the core, the authors also noted that fewer diatom valves were counted at lower depths. However, there is no specific detail on what samples these correspond to, and neither valve concentrations, nor the amount of sediment processed, are given. Due to the low organic carbon values in the lower part of their core, it can be assumed that their diatom concentrations also decreased with core depth. However, the top 10 cm corresponds well with our other observations of organic matter content and faunal subfossil remains, namely the diatom concentration in Mon1B following the increasing TC trend. Relatively high valve abundance over 1×10^9 g^{-1} suggests that a high proportion of the sediment in Unit 2 is of autochthonous origin. The scarcity of diatoms below 10 cm matches the lithological boundary between Units 1 and 2, and furthermore corresponds with the shift in diatom assemblage structure reported in Björck et al. (1996). While we did not characterise assemblages at these greater depths, we found most of the diatoms in the top layers were from the genus *Nitzschia,* and to a lesser degree *Staurosira,* which broadly corresponds to the results of Björck et al. (1996).

The most abundant species of core Mon1B was *Staurosirella frigida*, representing 21.4% of all counted valves. Due to past species force-fitting, all *Staurosirella* populations in the Maritime Antarctic Region had been previously grouped under *Staurosirella (Fragilaria) pinnata,* making it impossible to determine the exact distribution of the new species (Van de Vijver et al., 2014). In an analysis of recent material published by Kopalová et al. (2013), this species was observed only in the epilithon samples of Monolith Lake, with a relative abundance of 1.2% of all valves counted. However, no species of *Staurosirella* was reported in Björck et al. (1996), and likely this species is instead reported as either *Achnanthes exigua* or *A. conspicua*, given the high reported relative abundances of these latter taxa in their report, and the much lower counts of *Achnanthes* spp. in ours.

The next most abundant species were *Nitzschia kleinteichiana* (21.2%) and *Nitzschia annewillemsiana* (17.9%). Interestingly, the relative abundance of these species was inversely correlated. For example, *Nitzschia kleinteichiana* has its peak at 2–3 cm, where it represents almost 50% of the counts, in comparison with *Nitzschia annewillemsiana*, where this species represents only 0.02% (see Fig. 6). For submerged habitats, *Nitzschia kleinteichiana* seems to be one of the most representative, and largely reflects the contribution of epilithon (Kopalová et al., 2019). Both *Nitzschia* species are typical for stream and pond environments, exhibiting a broad ecological niche (Bulínová et al., 2020), and represent two of the most common *Nitzschia* species in the Maritime Antarctic Region (Zidarova et al., 2016). Previously, those species were included in the *Nitzschia perminuta* complex (as reported in Björck et al., 1996) and later split by Hamsher et al. (2016) into several species using the modern fine-grain taxonomy. In Kopalová et al. (2013), the most abundant epipelon species of the recent flora of Monolith Lake was *Humidophila australis*, with 24% of all valves counted. This species was reported as *Diadesmis perpusilla* in Björck et al. (1996) and, interestingly, it seemed to be either very rare or absent in the top layers, but increased in abundance with core depth. This was followed by the two *Nitzschia* species, with *Nitzschia annewillemsiana* representing 23% of the counts and *Nitzschia kleinteichiana* 14%.

Recent studies utilizing updated taxonomical concepts have been published from two lakes on nearby Vega Island with the aim to reconstruct their histories (Píšková et al., 2019; Čejka et al., 2020), along with a study that paired corresponding recent material to aid ecological interpretation (Bulínová et al., 2020). Strikingly, almost twice the diversity that was reported in Björck et al. (1996) was observed in Lake Esmeralda, with a diverse flora of 86 taxa described (Píšková et al., 2019) and 80 species were observed in Lake Anónima (Čejka et al. (2020). In the present reinvestigation of Monolith Lake, we found only 29 diatom taxa. This is comparable to the 35 taxa reported from recent samples in Kopalová et al. (2013), but direct comparison with the findings of Björck et al. (1996) is more difficult because of differences in

taxonomic concepts used. However, only a limited number of species in the Vega Island lakes reached significant abundances, suggesting that higher species richness might be simply attributed to more dynamic sedimentation processes which result in greater allochthonous inputs from the surrounding catchment area, and is further evidenced by the presence of semi-terrestrial species.

Subfossil crustaceofauna of Monolith Lake consisted of the fairy shrimp *Branchinecta gaini* and the calanoid copepod *Boeckella poppei*. Both species have been commonly reported during limnological surveys on JRI (including Monolith Lake) and the nearby Vega Island since 2008 (Nedbalová et al., 2017b). *B. gaini* was already recorded in sediments of Monolith Lake and two other JRI lakes (Dan [Keyhole] Lake and Hidden Lake) by Björck et al. (1996), who dated the colonisation by *B. gaini* to ~4 ka BP within local climatic optimum (in Monolith Lake itself to ~2 ka BP), and prevailed therein until the Neoglacial. The oldest record of *B. gaini* comes from Dan Lake, where the fairy shrimp was present until the lake dried out 3–2.5 ka BP. Hidden Lake, situated on the western side of JRI, hosted *B. gaini* between 2.5 and 1.5 ka BP. The disappearance of *B. gaini* from this lake was attributed to the onset of glaciolacustrine sedimentation during the Neoglacial, characterised by a high input of inorganic particles limiting microbial mat growth and thus limiting potential food sources. Also, Björck et al. (1996) associated the Neoglacial cooling that shortened the temporal window of liquid water availability vital for completing the life cycle of *B. gaini,* with its disappearance in Monolith Lake in the last ~1.5 ka. However, *B. gaini* did not disappear in the uppermost part of the sediment core analysed by Björck et al. (1996), although this section was affected by sediment loss during the coring (as already discussed in detail in the part 4.1.). The conclusion that B. *gaini* was extinct from JRI, which was later adopted by other authors, e.g. Gibson and Bayly (2007), was thus built upon a lack of field observation of *B. gaini* in the North-east Antarctic Peninsula bioregion and not on the palaeolimnological record. Uninterrupted occurrences of *Branchinecta gaini* in Monolith Lake in the last ~2.2 ka, as documented in this study, fills this gap. Nevertheless, in order to rule out the possibility of the Neoglacial extinction of *B. gaini* in the North-east Antarctic Peninsula region, more palaeolimnological data and sediment records covering the expected Neoglacial period are needed. Today, there is no evidence that *B. gaini* lives in permanently frozen lakes (Nedbalová et al., 2013). The continuous presence of *B. gaini* cysts in the Unit 2 of the core thus indicates the presence of at least infrequent longer ice-free periods during Antarctic summer through the past 2000 years (Hawes et al., 2008).

The second crustacean, *B. poppei*, was documented in sediments of JRI for the very first time. Although its remains were rather rare and missing in some depths of Unit 2, this scarcity could result from taphonomic processes, as most eggs were partially degraded. Also, the absence of spermatophores in at least the topmost layer was surprising since these were encountered in sediments of other lakes in the region inhabited by *B. poppei* (Gibson and Zale, 2006; Píšková et al., 2019). The colonisation potential and ecological valence of this crustacean are wider than that of *B. gaini* (e.g., Priddle and Heywood, 1980), and it seems plausible that *B. poppei* colonised Monolith Lake simultaneously as *B. gaini,* and has inhabited the lake for the last 2000 years just as the fairy shrimp has.

Rotifers were represented by loricae of *Notholca* sp., not very abundant and restricted only to the upper 6 cm of the sediment (the last ~800 years), a period with the highest TC, and ergo organic C content.

At least four species of tardigrades were recorded in the sediment of Monolith Lake. By far, the most abundant was a freshwater species *Dactylobiotus* cf. *ambiguus,* commonly recorded in lake sediments of Maritime Antarctica (Gibson et al., 2007; Cromer et al., 2008). Abundances of *Dactylobiotus* cf. *ambiguus* in Monolith Lake were the highest ever recorded among tardigrades in Antarctic Lake sediments (up to 6000 eggs g^{-1}), an order of magnitude higher than in Lake Boeckella (Hope Bay) and Limnopolar Lake (Livingston Island), where this species was previously recorded. Two more species known from the sediment of Lake Boeckella were found in Monolith Lake; the most abundant and widespread Antarctic tardigrade species, the limno-terrestrial *Acutuncus antarcticus*, was found here in low numbers, and the terrestrial *Mesobiotus furciger*, represented by a sole egg in section 0–1 cm. Apart from these shared species, the record of Monolith Lake included one egg of *Mesobiotus* cf. *blocki*, a fairly surprising discovery since this species has been reported only from East Antarctica (Guidetti et al., 2021), including lake sediments (Terrasovoje Lake, Amery Oasis; Gibson et al., 2007; Cromer et al., 2008), and two types of unidentified ornamented tardigrade eggs (see Appendix B).

5.3. Comparison with palaeoenvironmental reconstructions from Antarctic Peninsula

The Mid-Late Holocene Hypsithermal in the Antarctic Peninsula is most often constrained to 5–2 ka BP (Björck et al., 1996; Mulvaney et al., 2012; Sterken et al., 2012; Hodgson et al., 2013; Roberts et al., 2017; Kaplan et al., 2020), shortly before the regional onset of the Neoglacial cooling at 2.07 ± 0.05 ka BP (Čejka et al., 2020). Mulvaney et al. (2012) inferred from δD proxy in JRI ice core that temperatures marginally warmer than present lasted from 5 to 3 ka BP. Marine sedimentary record from Herbert Sound, between JRI and Vega Island (Minzoni et al., 2015), suggests a longer duration of warm, productive Mid-Holocene conditions ~7 to 2.5 ka. Kaplan et al. (2020) inferred the peak warmth on the James Ross Archipelago at 4–3 ka BP from terrestrial cosmogenic nuclide (TCN) dating of erratic boulders left by glacier retreat. Further south in the Larsen A and B embayments, TCN-based deglaciation chronologies reveal Mid-Holocene glacier surface lowering at ~4.5–3.5 ka (Balco et al., 2013) and between ~5 and 2–1 ka (Jeong et al., 2018). Similarly, Hypsithermal conditions are evidenced by proxies indicating a more humid and warmer climate in Monolith and Dan Lakes, including higher diatom and *B. gaini* concentrations, and less salt precipitation (Björck et al., 1996). Increased organic content and lake productivity, hence warmer conditions between ~3 and ~2.1 cal ka BP were also inferred for lakes on Beak Island (Sterken et al., 2012) and Vega Island (Čejka et al., 2020). Together with ^{36}Cl exposure dating evidence of the Lookalike Glacier recession (Jennings et al., unpublished data), the Mid-Late Holocene Hypsithermal appears to be a period of highly negative mass balance and rapid glacier retreat and down-wasting in the central part of the Ulu Peninsula, JRI, endorsing the inference of Monolith Lake formation and deposition of Unit 1 between ~2.5 and ~2.2 ka.

The Neoglacial period is characterised by climate cooling (Mulvaney et al., 2012; Čejka et al., 2020) and glacier advances (Carrivick et al., 2012; Kaplan et al., 2020; Heredia Barión et al., 2023b; Oliva et al., 2023; Theilen et al., 2023; Jennings et al., unpublished data). Monolith Lake reflected these environmental changes imminently in its abrupt lithological change, as the boundary between Units 1 and 2 is placed at ~2.2 ka BP (Fig. 8), which correlates with records from the eastern Antarctic Peninsula region (Pudsey and Evans, 2001; Mulvaney et al., 2012; Sterken et al., 2012; Čejka et al., 2020). In our view, the inferred reduced deposition in Monolith Lake is connected with proglacial hydrological changes and decreased meltwater input from the receding Lookalike Glacier, and longer or perhaps perennial ice-cover of the lake, during the coldest phases of the Neoglacial. Björck et al. (1996) also mentioned the possibility of perennial ice-cover and lake bottom-freezing, suggesting sediment erosion generating a hiatus. Cessation of accumulation could also result from desiccation or lake level lowering (amplifying the influence of bottom-freezing), both common occurrences in JRI and nearby lakes (Kavan, et al., 2021). Regarding local palaeoglaciological changes, Davies et al. (2014) presented a climatically driven model of the Neoglacial Lookalike Glacier re-advance to the Brandy Bay area. However, the deglaciation chronology presented here does not lend support to the timing of the modelled re-advance (Davies et al., 2014), as the glacier advance would have overrun the Monolith Lake basin and destroyed any previously

deposited lacustrine facies.

The last ~2200 years of our record document progressively increasing organic content and bioproductivity, connected with lake ontogeny and natural postglacial colonisation and succession of lacustrine microflora and invertebrates. Thus, a climate forcing of proxies must be interpreted carefully in the case of Unit 2 of the Monolith Lake sequence due to natural lake ontogeny influencing the sedimentation. The increase in diatom productivity and microfaunal abundance and species richness was possibly stimulated by a reduction in turbidity and concomitant increased light penetration, and lengthening of ice-free periods. Turbidity levels may have also dropped due to a reduction in glacier runoff associated with the Neoglacial cooling, or the aforementioned re-routing of glacial meltwater streams. The Monolith Lake record thus presents new long-term evidence of changes in the terrestrial biosphere, comparable to the 'greening of Antarctica' (i.e. growth of moss banks and associated microbial productivity over the last 50 years) observed in response to a warming climate (Amesbury et al., 2017). Our novel, lacustrine perspective suggests that increases in bioproductivity, once set in motion by favourable conditions (climate-induced deglaciation), may be sustained spontaneously (due to lake ontogeny) even on longer (millennial) timescales.

Concerning regional palaeoclimate, the Late Holocene temperature trends were highly variable owing to several competing driving factors (Vorrath et al., 2023). These include decreasing solar irradiance, Southern Hemisphere westerly wind field shifts over the Holocene, and differing conditions across the east-west divide of the Antarctic Peninsula orographic barrier, in addition to complex physiography of glaciers, marine bays and lakes, where the palaeorecords have been collected (Mulvaney et al., 2012; Totten et al., 2022; Heredia Barión et al., 2023a). The asynchronous onset and duration of the Neoglacial events may also stem from varied geographical foci and longevity of the climate forcings (Totten et al., 2022), with the interplay of Circumpolar Deep Water upwelling, Southern Annular Mode (affecting the strength and position of the southern westerlies and Weddell Gyre), and the El Niño Southern Oscillation all contributing to a still incomplete picture of the long-term mechanisms of change (Kaplan et al., 2020; van der Bilt et al., 2022; Heredia Barión et al., 2023a, 2023b). Nonetheless, within the last millennium, episodically increasing temperatures have been inferred in the eastern Antarctic Peninsula from lake sediments (Björck et al., 1996; Sterken et al., 2012), and later, after ~0.5 ka BP, ice-core palaeoreconstructions (Mulvaney et al., 2012). Emerging evidence of the Neoglacial re-advances around the Antarctic Peninsula within the several last centuries (Kaplan et al., 2020; Simms et al., 2021; Totten et al., 2022; Heredia Barión et al., 2023b), comparable to the Northern Hemisphere "Little Ice Age", may in fact signify the terminal phase of the Neoglacial (Mulvaney et al., 2012; Oliva et al., 2016; Palacios et al., 2020; Theilen et al., 2023) and the onset of the glacier retreat, thus leaving the large moraine complexes speckled with TCN-dateable erratics found on the maximum advance positions (Jennings et al., unpublished data). The transverse ridges on the JRI moraine complexes may reflect multiple small advances associated with the Little Ice Age from ~0.5 to ~0.3 ka BP (Carrivick et al., 2012; Kaplan et al., 2020). However, no sedimentary evidence suggests that the Lookalike Glacier has reached the position of Monolith Lake during these Late Neoglacial re-advances despite its current front being located <3 km from Monolith Lake.

The small decrease in bioproductivity seen in both diatoms and faunal subfossils and TC and TN proxies near the top of Monolith Lake cores may reflect these colder conditions, or rather amplified climatic oscillations, of the last several centuries. Nevertheless, the overall climatic trends since at least the mid-20th century, termed the Recent Rapid Regional warming (Bentley et al., 2009), have led to widespread changes in the terrestrial ecosystems, manifested in increased biological activity or ecological shifts across the Antarctic Peninsula region (Quayle et al., 2002; Amesbury et al., 2017; Lee et al., 2017; Heredia Barión et al., 2023a).

6. Conclusions

Monolith Lake, located on the Ulu Peninsula, JRI, is a proglacial lake in one of the largest ice-free areas in the Antarctic Peninsula region. A lacustrine sedimentary sequence was recovered, comprehensively dated and analysed in a multi-proxy approach to characterise abiotic and biotic palaeoenvironmental changes. The lowermost parts of the cores studied (Unit 1) exhibit a homogeneous composition and unvarying proxy data profiles, suggesting a rapid deposition under uniform conditions in a glacioproximal setting. The ^{14}C and SAR-OSL dating brackets the interval of deposition to 1.5–2.5 ka BP, with the older age being more probable due to pitfalls of bulk sediment ^{14}C dating in the Antarctic and thanks to independent dating control of local deglaciation. Therefore, we consider a much shorter duration of this phase, very likely in the interval 2.2–2.5 ka BP. The topmost 11 cm (Unit 2) were deposited in the last ~2.2 ka BP (i.e. the Neoglacial Period) and document the lower accumulation rate and increasingly higher biogenic sedimentation, attributed to diminished influence of glacial meltwater sources and turbidity decrease associated with the reduced glacier runoff, respectively. Nonetheless, natural lake ontogeny (i.e. the progressive increase in organic productivity) seems to prevail over the effects of the Neoglacial cooling. Shortly after the cessation of rapid sediment accumulation, Monolith Lake was colonised by crustaceans *B. gaini* and *B. poppei*. Throughout the subsequent period, Monolith Lake hosted a community of benthic diatoms with fluctuating but overall stable species composition, and a diverse faunal community of the above-mentioned crustaceans, rotifers *Notholca* sp., and multiple tardigrade species dominated by *Dactylobiotus* cf. *ambiguus*. Both the diatom and faunal records remained uninterrupted to the present day, which supports the existence of a biodiversity hotspot even during the coldest phases of the Neoglacial Period and the recent rapid regional warming, and corroborate the Antarctic 'greening' narrative from a lacustrine perspective.

Author contributions

Conceptualisation: DN, MR, KK, Field work: DN, JK, MR, Investigation: MR, AP, DCWS, AC, MB, MP, VS, KK, Supervision: DN, KK, LN, VS, DCWS, Formal Analysis: MR, Visualisation: MR, Writing – original draft: MR, MP, AP, KK, Writing – review and editing: MR, AP, DCWS, AC, MB, MP, JK, SJAJ, JML, LN, VS, KK, NFG, DN.

Declaration of competing interest

The authors declare that they have no known competing financial interests or personal relationships that could have appeared to influence the work reported in this paper.

Data availability

Satellite and geospatial data used in the study are publicly available from Sentinel Hub (https://www.sentinel-hub.com/), Polar Geospatial Center (https://www.pgc.umn.edu/data/rema/), SCAR Antarctic Digital Database (http://www.add.scar.org/) and Norsk Polar Institut (https://www.npolar.no/quantarctica/). The datasets presented in this study can be found in the Supplementary materials.

Acknowledgements

This work has been supported by Charles University Research Centre program No. 204069, the Charles University GAUK project No. 981118, the Czech Science Foundation (GAČR) projects No. 16-17346Y and 22-20621O, and the institutional long-term research plan of the Institute of Botany of Czech Academy of Sciences (RVO 67985939). The authors appreciate the use of the Czech Antarctic Research Programme infrastructure, supported by the MEYS projects VAN2022/1, VAN 2021/1,

VAN 2020/1, LM2015078, CZ.02.2.69/0.0/0.0/16_027/0008360, and CZ.02.1.01/0.0/0.0/16_013/0001708, as well as the J. G. Mendel Station, and acknowledge its staff for all the support they provided. MR's contribution was supported by JCMM Brno PhD Talent and Geo-Excellence scholarships. We would like to acknowledge Tyler J. Kohler and Daniel Vondrák for their valuable advice. We would also like to thank Dominic Hodgson, Stephen Roberts, and anonymous reviewers for their constructive comments, which greatly improved the original manuscript.

Appendix A. Supplementary data

Supplementary data to this article can be found online at https://doi.org/10.1016/j.quascirev.2024.108693.

References

Amesbury, M.J., Roland, T.P., Royles, J., Hodgson, D.A., Convey, P., Griffiths, H., Charman, D.J., 2017. Widespread biological response to rapid warming on the Antarctic Peninsula. Curr. Biol. 27, 1616–1622.

Antoniades, D., Giralt, S., Geyer, A., Álvarez-Valero, A.M., Pla-Rabes, S., Granados, I., Liu, E.J., Toro, M., Smellie, J.L., Oliva, M., 2018. The timing and widespread effects of the largest Holocene volcanic eruption in Antarctica. Sci. Rep. 8, 17279.

Balascio, N.L., D'Andrea, W.J., Bradley, R.S., Perren, B.B., 2013. Biogeochemical evidence for hydrologic changes during the Holocene in a lake sediment record from southeast Greenland. Holocene 23, 1428–1439.

Balco, G., Schaefer, J.M., Larissa, 2013. Exposure-age record of Holocene ice sheet and ice shelf change in the northeast Antarctic Peninsula. Quat. Sci. Rev. 59, 101–111.

Barták, M., Váczi, P., Stachoň, Z., Kubešová, S., 2015. Vegetation mapping of moss-dominated areas of northern part of James Ross Island (Antarctica) and a suggestion of protective measures. Czech Polar Rep 5, 75–87.

Baumhoer, C.A., Dietz, A.J., Kneisel, C., Paeth, H., Kuenzer, C., 2021. Environmental drivers of circum-Antarctic glacier and ice shelf front retreat over the last two decades. Cryosphere 15, 2357–2381.

Bentley, M.J., Hodgson, D.A., Smith, J.A., Cofaigh, C., Domack, E.W., Larter, R.D., Roberts, S.J., Brachfeld, S., Leventer, A., Hjort, C., Hillenbrand, C.-D., Evans, J., 2009. Mechanisms of Holocene palaeoenvironmental change in the Antarctic Peninsula region. Holocene 19, 51–69.

Bird, M.I., Chivas, A.R., Radnell, C.J., Burton, H.R., 1991. Sedimentological and stable-isotope evolution of lakes in the Vestfold Hills, Antarctica. Palaeogeogr. Palaeoclimatol. Palaeoecol. 84, 109–130.

Björck, S., Hjort, C., Ingólfsson, Ó., Skog, G., 1991. Radiocarbon dates from the Antarctic Peninsula region – problems and potential. Quat. Proc. 1, 55–65.

Björck, S., Olsson, S., Ellis-Evans, C., Håkansson, H., Humlum, O., Lirio, J.M., 1996. Late Holocene palaeoclimatic records from lake sediments on James Ross Island, Antarctica. Palaeogeogr. Palaeoclimatol. Palaeoecol. 121, 195–220.

Blaauw, M., Christen, J.A., 2011. Flexible paleoclimate age-depth models using an autoregressive gamma process. Bayesian Anal 6, 457–474.

Blott, S.J., Pye, K., 2001. GRADISTAT: a grain size distribution and statistics package for the analysis of unconsolidated sediments. Earth Surf. Process. Landforms 26, 1237–1248.

Bøtter-Jensen, L., Bulur, E., Duller, G.A., Murray, A., 2000. Advances in luminescence instrument systems. Radiat. Meas. 32, 523–528.

Brachfeld, S., Domack, E., Kissel, C., Laj, C., Leventer, A., Ishman, S., Gilbert, R., Camerlenghi, A., Eglinton, L.B., 2003. Holocene history of the Larsen-A Ice Shelf constrained by geomagnetic paleointensity dating. Geology 31, 749–752.

Bronk Ramsey, C., 2009. Bayesian analysis of radiocarbon dates. Radiocarbon 51, 337–360.

Bulínová, M., Kohler, T.J., Kavan, J., Van de Vijver, B., Nývlt, D., Nedbalová, L., Coria, S. H., Lirio, J.M., Kopalová, K., 2020. Comparison of diatom paleo-assemblages with adjacent limno-terrestrial communities on Vega Island, Antarctic Peninsula. Water 12, 1340.

Calabozo, F.M., Strelin, J.A., Orihashi, Y., Sumino, H., Keller, R.A., 2015. Volcano-ice-sea interaction in the Cerro Santa Marta area, northwest James Ross Island, Antarctic Peninsula. J. Volcanol. Geoth. Res. 297, 89–108.

Carrivick, J.L., Davies, B.J., Glasser, N.F., Nývlt, D., Hambrey, M.J., 2012. Late-Holocene changes in character and behaviour of land-terminating glaciers on James Ross Island, Antarctica. J. Glaciol. 58, 1176–1190.

Čejka, T., Nývlt, D., Kopalová, K., Bulínová, M., Kavan, J., Lirio, J.M., Coria, S.H., Van de Vijver, B., 2020. Timing of the neoglacial onset on the North-Eastern Antarctic Peninsula based on lacustrine archive from Lake Anónima, Vega Island. Global Planet. Change 184, 103050.

Chinn, T.J.H., Dillon, A., 1987. Observations on a debris-covered polar glacier 'Whisky Glacier', James Ross Island, Antarctic Peninsula, Antarctica. J. Glaciol. 33, 300–310.

Chown, S.L., Clarke, A., Fraser, C.I., Cary, S.C., Moon, K.L., McGeoch, M.A., 2015. The changing form of Antarctic biodiversity. Nature 522, 431–438.

Cook, A.J., Vaughan, D.G., 2010. Overview of areal changes of the ice shelves on the Antarctic Peninsula over the past 50 years. Cryosphere 4, 77–98.

Cromer, L., Gibson, J.A.E., McInnes, S.J., Agius, J.T., 2008. Tardigrade remains from lake sediments. J. Paleolimnol. 39, 143–150.

Czech Geological Survey, 2009. James Ross Island – Northern Part. Topographic Map 1: 25 000, first ed. Czech Geological Survey, Praha.

Davies, B.J., Glasser, N.F., Carrivick, J.L., Hambrey, M.J., Smellie, J.L., Nývlt, D., 2013. Landscape evolution and ice-sheet behaviour in a semi-arid polar environment: James Ross Island, NE Antarctic Peninsula. Geol. Soc. London, Spec. Publ. 381, 353–395.

Davies, B.J., Golledge, N.R., Glasser, N.F., Carrivick, J.L., Ligtenberg, S.R.M., Barrand, N. E., van den Broeke, M.R., Hambrey, M.J., Smellie, J.L., 2014. Modelled glacier response to centennial temperature and precipitation trends on the Antarctic Peninsula. Nat. Clim. Change 4, 993–998.

DeConto, R.M., Pollard, D., Alley, R.B., Velicogna, I., Gasson, E., Gomez, N., Sadai, S., Condron, A., Gilford, D.M., Ashe, E.L., Kopp, R.E., Li, D., Dutton, A., 2021. The Paris Climate Agreement and future sea-level rise from Antarctica. Nature 593, 83–89.

Engel, Z., Láska, K., Nývlt, D., Stachoň, Z., 2018. Surface mass balance of small glaciers on James Ross Island, north-eastern Antarctic Peninsula, during 2009-2015. J. Glaciol. 64, 349–361.

Engel, Z., Nývlt, D., Láska, K., 2012. Ice thickness, areal and volumetric changes of Davies Dome and Whisky Glacier in 1979–2006 (James Ross Island, Antarctic Peninsula). J. Glaciol. 58, 904–914.

Esposito, R.M.M., Spaulding, S.A., McKnight, D.M., Van de Vijver, B., Kopalová, K., Lubinski, D., Hall, B., Whittaker, T., 2008. Inland diatoms from the McMurdo Dry Valleys and James Ross Island, Antarctica. Botany 86, 1378–1392.

Folk, R.L., Ward, W.C., 1957. Brazos River bar: a study in the significance of grain size parameters. J. Sediment. Res. 27, 3–26.

Francis, J.E., Crame, J.A., Pirrie, D., 2006. Cretaceous-Tertiary high-latitude palaeoenvironments, James Ross Basin, Antarctica: introduction. Geol. Soc. London, Spec. Publ. 258, 1–5.

Fritz, S.C., Anderson, N.J., 2013. The relative influences of climate and catchment processes on Holocene lake development in glaciated regions. J. Paleolimnol. 49, 349–362.

Gibson, J.A.E., Bayly, I.A.E., 2007. New insights into the origins of crustaceans of Antarctic lakes. Antarct. Sci. 19, 157–164.

Gibson, J.A.E., Cromer, L., Agius, J.T., Mcinnes, S.J., Marley, N.J., 2007. Tardigrade eggs and exuviae in Antarctic lake sediments: insights into Holocene dynamics and origins of the fauna. J. Limnol. 66, 65.

Gibson, J.A.E., Wilmotte, A., Taton, A., Van de Vijver, B., Beyens, L., Dartnall, H., 2006. Biogeographic trends in Antarctic lake communities. In: Bergstrom, D.M., Convey, P., Huiskes, A.H.L. (Eds.), Trends Antarct. Terr. Limnetic Ecosyst 71–99.

Gibson, J.A.E., Zale, R., 2006. Holocene development of the fauna of Lake Boeckella, northern Antarctic Peninsula. Holocene 16, 625–634.

Giralt, S., Hernández, A., Pla-Rabés, S., Antoniades, D., Toro, M., Granados, I., Oliva, M., 2020. Holocene environmental changes inferred from Antarctic lake sediments. In: Oliva, M., Ruiz-Fernández, J. (Eds.), Past Antarctica, Palaeoclimatology and Climate Change. Academic Press, London, UK, pp. 51–66.

Glasser, N.F., Davies, B.J., Carrivick, J.L., Rodés, A., Hambrey, M.J., Smellie, J.L., Domack, E., 2014. Ice-stream initiation, duration and thinning on James Ross island, northern Antarctic Peninsula. Quat. Sci. Rev. 86, 78–88.

Glew, J.R., Smol, J.P., Last, W.M., 2002. Sediment core collection and extrusion. In: Last, W.M., Smol, J.P. (Eds.), Tracking Environmental Change Using Lake Sediments, Volume 1: Basin Analysis, Coring, and Chronological Techniques. Kluwer, Dordrecht, pp. 73–105. Developments in Paleoenvironmental Research.

Gore, D.B., 1997. Blanketing snow and ice; constraints on radiocarbon dating deglaciation in East Antarctic oases. Antarct. Science 9, 336–346.

Grygar, T., Bláhová, A., Hradil, D., Bezdička, P., Kadlec, J., Schnabl, P., Swann, G., Oberhänsli, H., 2007. Lake Baikal climatic record between 310 and 50 ky BP: interplay between diatoms, watershed weathering and orbital forcing. Palaeogeogr. Palaeoclimatol. Palaeoecol. 250, 50–67.

Grygar, T., Kadlec, J., Žigová, A., Mihaljevič, M., Nekutová, T., Lojka, R., Světlík, I., 2009. Chemostratigraphic correlation of sediments containing expandable clay minerals based on ion exchange with Cu(II) triethylenetetramine. Clay Clay Miner. 57, 168–182.

Guidetti, R., McInnes, S.J., Kristensen, R.M., 2021. World list of tardigrada. *Mesobiotus Blocki* (Dastych, 1984). http://www.marinespecies.org/tardigrada/aphia.php?p=taxdetails&id=886406on2022-03-23.

Håkansson, H., Olsson, S., Björck, S., 1995. Diatom record and sediment chemistry of a shallow, glaciolacustrine basin on James Ross Island, Antarctica. PACT 50, 417–430.

Hamilton, P., De Haan, M., Kopalová, K., Zidarova, R., Van de Vijver, B., 2014. An evaluation of selected *Neidium* species from the Antarctic Region. Diatom Res. 29, 27–40.

Hamsher, S., Kopalová, K., Kociolek, P.J., Zidarova, R., Van de Vijver, B., 2016. The genus *Nitzschia* on the south Shetland Islands and James Ross Island (maritime Antarctica). Fottea 16, 79–102.

Hansson, L.-A., Håkansson, H., 1992. Diatom community response along a productivity gradient of shallow Antarctic lakes. Polar Biol. 12, 463–468.

Hawes, I, Brazier, P, 1991. Freshwater stream ecosystems of James Ross Island, Antarctica. Antarct. Sci. 3, 265–271.

Hawes, T.C., Worland, M.R., Bale, J.S., 2008. Physiological constraints on the life cycle and distribution of the Antarctic fairy shrimp *Branchinecta gaini*. Polar Biol. 31, 1531–1538.

Hendy, C.H., Hall, B.L., 2006. The radiocarbon reservoir effect in proglacial lakes: examples from Antarctica. Earth Planet Sci. Lett. 241, 413–421.

Heredia Barión, P., Roberts, S.J., Spiegel, C., Binnie, S.A., Wacker, L., Davies, J., Gabriel, I., Jones, V.J., Blockley, S., Pearson, E.J., Foster, L., Davies, S.J., Roland, T. P., Hocking, E.P., Bentley, M.J., Hodgson, D.A., Hayward, C.L., McCulloch, R.D., Strelin, J.A., Kuhn, G., 2023a. Holocene deglaciation and glacier readvances on the

Fildes Peninsula and King George Island (Isla 25 de Mayo), South Shetland Islands, NW Antarctic Peninsula. Holocene 33, 636–658.
Heredia Barión, P.A., Strelin, J.A., Roberts, S.J., Spiegel, C., Wacker, L., Niedermann, S., Bentley, M.J., Pearson, E.J., Czalbowski, N.T.M., Davies, S.J., Schnetger, B., Grosjean, M., Arcusa, S., Perren, B., Hocking, E.P., Kuhn, G., 2023b. The impact of Holocene deglaciation and glacial dynamics on the landscapes and geomorphology of Potter Peninsula, King George Island (Isla 25 Mayo), NW Antarctic Peninsula. Front. Earth Sci. 10, 1073075.
Hjort, C., Ingólfsson, Ó., Möller, P., Lirio, J.M., 1997. Holocene glacial history and sea-level changes on James Ross Island, Antarctic Peninsula. J. Quat. Sci. 12, 259–273.
Hodgson, D.A., Doran, P.T., Roberts, D., McMinn, A., 2004. Paleolimnological studies from the Antarctic and subantarctic islands. In: Pienitz, R., Douglas, M.S.V., Smol, J. P. (Eds.), Long-term Environmental Change in Arctic and Antarctic Lakes. Springer, Dordrecht, pp. 419–474.
Hodgson, D.A., Roberts, S.J., Bentley, M.J., Carmichael, E.L., Smith, J.A., Verleyen, E., Vyverman, W., Geissler, P., Leng, M.J., Sanderson, D.C.W., 2009. Exploring former subglacial Hodgson Lake, Antarctica. Paper II: palaeolimnology. Quat. Sci. Rev. 28, 2310–2325.
Hodgson, D.A., Roberts, S.J., Smith, J.A., Verleyen, E., Sterken, M., Labarque, M., Sabbe, K., Vyverman, W., Allen, C.S., Leng, M.J., Bryant, C., 2013. Late Quaternary environmental changes in Marguerite Bay, Antarctic Peninsula, inferred from lake sediments and raised beaches. Quat. Sci. Rev. 68, 216–236.
Hogg, A.G., Heaton, T.J., Hua, Q., Palmer, J.G., Turney, C.S.M., Southon, J., Bayliss, A., Blackwell, P.G., Boswijk, G., Bronk Ramsey, C., Pearson, C., Petchey, F., Reimer, P., Reimer, R., Wacker, L., 2020. SHCal20 Southern Hemisphere calibration, 0–55,000 years cal BP. Radiocarbon 62, 759–778.
Howat, I.M., Porter, C., Smith, B.E., Noh, M.-J., Morin, P., 2019. The Reference Elevation Model of Antarctica. Cryosphere 13, 665–674.
Hrbáček, F., Uxa, T., 2020. The evolution of a near-surface ground thermal regime and modelled active-layer thickness on James Ross Island, Eastern Antarctic Peninsula, in 2006–2016. Permafr. Periglac. Process. 31, 141–155.
Ingólfsson, Ó., Hjort, C., Berkman, P.A., Björck, S., Colhoun, E., Goodwin, I.D., Hall, B., Hirakawa, K., Melles, M., Möller, P., Prentice, M.L., 1998. Antarctic glacial history since the Last Glacial Maximum: an overview of the record on land. Antarct. Sci. 10, 326–344.
Jennings, S.J.A., Davies, B.J., Nývlt, D., Glasser, N.F., Engel, Z., Hrbáček, F., Carrivick, J. L., Mlčoch, B., Hambrey, M.J., 2021. Geomorphology of Ulu Peninsula, James Ross Island, Antarctica. J. Maps 17, 125–139.
Jennings, S.J.A., Hambrey, M.J., 2021. Structures and deformation in glaciers and ice sheets. Rev. Geophys. 59, 1–135.
Jennings, S.J.A., Nývlt, D., Roman, M., Davies, B.J., Glasser, N.F., Carrivick, J.L., Hambrey, M.J. Mid- to late-Holocene deglaciation chronology from ^{36}Cl cosmogenic nuclide dating of basalt erratics, James Ross Island, Antarctic Peninsula (in prep.).
Jeong, A., Lee, J. Il, Seong, Y.B., Balco, G., Yoo, K.C., Yoon, H. Il, Domack, E., Rhee, H.H., Yu, B.Y., 2018. Late Quaternary deglacial history across the Larsen B embayment, Antarctica. Quat. Sci. Rev. 189, 134–148.
Johnson, J.S., Bentley, M.J., Roberts, S.J., Binnie, S.A., Freeman, S.P.H.T., 2011. Holocene deglacial history of the northeast Antarctic Peninsula – A review and new chronological constraints. Quat. Sci. Rev. 30, 3791–3802.
Juggins, S., 2017. Rioja: analysis of quaternary science data. R Package Version 0. 9–26. Available at: https://cran.r-project.Org/web/packages/rioja/index.html.
Kaplan, M.R., Strelin, J.A., Schaefer, J.M., Peltier, C., Martini, M.A., Flores, E., Winckler, G., Schwartz, R., 2020. Holocene glacier behavior around the northern Antarctic Peninsula and possible causes. Earth Planet Sci. Lett. 534, 116077.
Karlén, W., Hjort, C., Ingólfsson, Ó., Zale, R., 1988. Holocene glacial history and climate variation on the Antarctic Peninsula. Ber. Polarforsch. 58, 40–41.
Kavan, J., 2017. Water temperature regime of selected lakes on James Ross Island during 2015 austral summer. Czech Polar Reports 7, 83–93.
Kavan, J., Nedbalová, L., Nývlt, D., Čejka, T., Lirio, J.M., 2021. Status and short-term environmental changes of lakes in the area of Devil's Bay, Vega Island, Antarctic Peninsula. Antarct. Sci. 33, 150–164.
Kavan, J., Nývlt, D., Láska, K., Engel, Z., Kňažková, M., 2020. High-latitude dust deposition in snow on the glaciers of James Ross Island, Antarctica. Earth Surf. Process. Landforms 45, 1569–1578.
Kavan, J., Ondruch, J., Nývlt, D., Hrbáček, F., Carrivick, J.L., Láska, K., 2017. Seasonal hydrological and suspended sediment transport dynamics in proglacial streams, James Ross Island, Antarctica. Geogr. Ann. Ser. A 99, 38–55.
Kňažková, M., Hrbáček, F., Kavan, J., Nývlt, D., 2020. Effect of hyaloclastite breccia boulders on meso-scale periglacial-aeolian landsystem in semi-arid Antarctic environment, James Ross Island, Antarctic Peninsula. Cuadernos Invest. Geogr. 46, 7–31.
Komárek, J., Elster, J., Komárek, O., 2008. Diversity of the cyanobacterial microflora of the northern part of James Ross Island, NW Weddell Sea, Antarctica. Polar Biol. 31, 853–865.
Komárek, O., Komárek, J., 2010. Diversity and ecology of cyanobacterial microflora of the seepages habitat. Comparison of King George Island, Shetland Islands, and James Ross Island, NW Weddell Sea, Antarctica. In: Seckbach, J., Oren, A. (Eds.), Microbial Mats. Springer Verlag, pp. 517–539.
Kopalová, K., Elster, J., Komárek, J., Veselá, J., Nedbalová, L., Van de Vijver, B., 2012. Benthic diatoms (Bacillariophyta) from seepages and streams on James Ross Island (NW Weddell Sea, Antarctica). Plant Ecol. Evol. 145, 190–208.
Kopalová, K., Nedbalová, L., de Haan, M., Van de Vijver, B., 2011. Description of five new species of the diatom genus *Luticola* (Bacillariophyta, Diadesmidaceae) found in lakes of James Ross Island (Maritime Antarctic Region). Phytotaxa 27, 44–60.
Kopalová, K., Nedbalová, L., Nývlt, D., Elster, J., Van de Vijver, B., 2013. Diversity, ecology and biogeography of the freshwater diatom communities from Ulu Peninsula (James Ross Island, NE Antarctic Peninsula). Polar Biol. 36, 933–948.
Kopalová, K., Soukup, J., Kohler, T.J., Roman, M., Coria, S.H., Vignoni, P.A., Lecomte, K. L., Nedbalová, L., Nývlt, D., Lirio, J.M., 2019. Habitat controls on limno-terrestrial diatom communities of Clearwater Mesa, James Ross Island, Maritime Antarctica. Polar Biol. 42, 1595–1613.
Laybourn-Parry, J., Pearce, D.A., 2007. The biodiversity and ecology of Antarctic lakes: models for evolution. Philos. Trans. R. Soc. B Biol. Sci. 362, 2273–2289.
Lee, J.R., Raymond, B., Bracegirdle, T.J., Chadès, I., Fuller, R.A., Shaw, J.D., Terauds, A., 2017. Climate change drives expansion of Antarctic ice-free habitat. Nature 547, 49–54.
Levy, J.S., Rittenour, T.M., Fountain, A.G., O'Connor, J.E., 2017. Luminescence dating of paleolake deltas and glacial deposits in Garwood Valley, Antarctica: implications for climate, Ross ice sheet dynamics, and paleolake duration. Geol. Soc. Am. Bull. 129, B31539.1.
Matsuoka, K., Skoglund, A., Roth, G., de Pomereu, J., Griffiths, H., Headland, R., Herried, B., Katsumata, K., Le Brocq, A., Licht, K., Morgan, F., Neff, P.D., Ritz, C., Scheinert, M., Tamura, T., Van de Putte, A., van den Broeke, M., von Deschwanden, A., Deschamps-Berger, C., Van Liefferinge, B., Tronstad, S., Melvær, Y., 2021. Quantarctica, an integrated mapping environment for Antarctica, the Southern Ocean, and sub-Antarctic islands. Environ. Model. Software 140, 105015.
Michalchuk, B.R., Anderson, J.B., Wellner, J.S., Manley, P.L., Majewski, W., Bohaty, S., 2009. Holocene climate and glacial history of the northeastern Antarctic Peninsula: the marine sedimentary record from a long SHALDRIL core. Quat. Sci. Rev. 28, 3049–3065.
Minzoni, R.T., Anderson, J.B., Fernandez, R., Wellner, J.S., 2015. Marine record of Holocene climate, ocean, and cryosphere interactions: Herbert Sound, James Ross Island, Antarctica. Quat. Sci. Rev. 129, 239–259.
Mlčoch, B., Nývlt, D., Mixa, P., 2020. Geological Map of James Ross Island – Northern Part 1:25 000. Czech Geological Survey, Praha.
Morlighem, M., Rignot, E., Binder, T., Blankenship, D., Drews, R., Eagles, G., Eisen, O., Ferraccioli, F., Forsberg, R., Fretwell, P., Goel, V., Greenbaum, J.S., Gudmundsson, H., Guo, J., Helm, V., Hofstede, C., Howat, I., Humbert, A., Jokat, W., Karlsson, N.B., Lee, W.S., Matsuoka, K., Millan, R., Mouginot, J., Paden, J., Pattyn, F., Roberts, J., Rosier, S., Ruppel, A., Seroussi, H., Smith, E.C., Steinhage, D., Sun, B., van den Broeke, M.R., van Ommen, T.D., van Wessem, M., Young, D.A., 2020. Deep glacial troughs and stabilizing ridges unveiled beneath the margins of the Antarctic ice sheet. Nat. Geosci. 13, 132–137.
Mulvaney, R., Abram, N.J., Hindmarsh, R.C.A., Arrowsmith, C., Fleet, L., Triest, J., Sime, L., Alemany, O., Foord, S., 2012. Recent Antarctic Peninsula warming relative to Holocene climate and ice shelf history. Nature 488, 141–144.
Munyikwa, K., Kinnaird, T.C., Sanderson, D.C.W., 2021. The potential of portable luminescence readers in geomorphological investigations: a review. Earth Surf. Process. Landforms 46, 131–150.
Nedbalová, L., Mihál, M., Kvíderová, J., Procházková, L., Řezanka, T., Elster, J., 2017a. Identity, ecology and ecophysiology of planktic green algae dominating in ice-covered lakes on James Ross Island (northeastern Antarctic Peninsula). Extremophiles 21, 187–200.
Nedbalová, L., Nývlt, D., Kopáček, J., Šobr, M., Elster, J., 2013. Freshwater lakes of Ulu Peninsula, James Ross Island, North-east Antarctic Peninsula: origin, geomorphology and physical and chemical limnology. Antarct. Sci. 25, 358–372.
Nedbalová, L., Nývlt, D., Lirio, J.M., Kavan, J., Elster, J., 2017b. Current distribution of *Branchinecta gaini* on James Ross Island and Vega Island. Antarct. Sci. 29, 341–342.
Nehyba, S., Nývlt, D., 2014. Deposits of pyroclastic mass flows at Bibby Hill (Pliocene, James Ross Island, Antarctica). Czech Polar Reports 4, 103–122.
Noble, T.L., Rohling, E.J., Aitken, A.R.A., Bostock, H.C., Chase, Z., Gomez, N., Jong, L.M., King, M.A., Mackintosh, A.N., McCormack, F.S., McKay, R.M., Menviel, L., Phipps, S. J., Weber, M.E., Fogwill, C.J., Gayen, B., Golledge, N.R., Gwyther, D.E., Hogg, A.M., Martos, Y.M., Pena-Molino, B., Roberts, J., Flierdt, T., Williams, T., 2020. The sensitivity of the Antarctic Ice Sheet to a changing climate: past, present, and future. Rev. Geophys. 58, 1–89.
Nývlt, D., Braucher, R., Engel, Z., Mlčoch, B., ASTER Team, 2014. Timing of the northern Prince Gustav Ice Stream retreat and the deglaciation of northern James Ross Island, Antarctic Peninsula during the last glacial–interglacial transition. Quat. Res. 82, 441–449.
Nývlt, D., Fišáková Nývltová, M., Barták, M., Stachoň, Z., Pavel, V., Mlčoch, B., Láska, K., 2016. Death age, seasonality, taphonomy and colonization of seal carcasses from Ulu Peninsula, James Ross Island, Antarctic Peninsula. Antarct. Science 28, 3–16.
Nývlt, D., Glasser, N., Hocking, E., Oliva, M., Roberts, S.J., Roman, M., 2020. Tracing the deglaciation since the Last Glacial Maximum. In: Oliva, M., Ruiz-Fernández, J. (Eds.), Past Antarctica, Palaeoclimatology and Climate Change. Academic Press, London, UK, pp. 89–107.
Nývlt, D., Košler, J., Mlčoch, B., Mixa, P., Lisá, L., Bubík, M., Hendriks, B.W.H., 2011. The Mendel Formation: evidence for Late Miocene climatic cyclicity at the northern tip of the Antarctic Peninsula. Palaeogeogr. Palaeoclimatol. Palaeoecol. 299, 363–384.
Ó Cofaigh, C., Davies, B.J., Livingstone, S.J., Smith, J.A., Johnson, J.S., Hocking, E.P., Hodgson, D.A., Anderson, J.B., Bentley, M.J., Canals, M., Domack, E., Dowdeswell, J. A., Evans, J., Glasser, N.F., Hillenbrand, C.-D., Larter, R.D., Roberts, S.J., Simms, A. R., 2014. Reconstruction of ice-sheet changes in the Antarctic Peninsula since the Last Glacial Maximum. Quat. Sci. Rev. 100, 87–110.
Obu, J., Westermann, S., Vieira, G., Abramov, A., Balks, M.R., Bartsch, A., Hrbáček, F., Kääb, A., Ramos, M., 2020. Pan-Antarctic map of near-surface permafrost temperatures at 1 km^2 scale. Cryosphere 14, 497–519.

Oliva, M., Antoniades, D., Giralt, S., Granados, I., Pla-Rabes, S., Toro, M., Liu, E.J., Sanjurjo, J., Vieira, G., 2016. The Holocene deglaciation of the Byers Peninsula (Livingston Island, Antarctica) based on the dating of lake sedimentary records. Geomorphology 261, 89–102.
Oliva, M., Navarro, F., Hrbáček, F., Hernández, A., Nývlt, D., Pereira, P., Ruiz-Fernández, J., Trigo, R., 2017. Recent regional climate cooling on the Antarctic Peninsula and associated impacts on the cryosphere. Sci. Total Environ. 580, 210–223.
Oliva, M., Palacios, D., Fernández-Fernández, J.M., Fernandes, M., Schimmelpfennig, I., Vieira, G., Antoniades, D., Pérez-Alberti, A., García-Oteyza, J., Aumaître, G., Keddadouche, K., 2023. Holocene deglaciation of the northern Fildes Peninsula, King George Island, Antarctica. Land Degrad. Dev. 34, 3973–3990.
Øvstedal, D.O., Lewis-Smith, R.L., 2001. Lichens of Antarctica and South Georgia. A guide to their identification and ecology. Cambridge University Press, Cambridge, p. 424.
Palacios, D., Ruiz-Fernández, J., Oliva, M., Andrés, N., Fernández-Fernández, J.M., Schimmelpfennig, I., Leanni, L., González-Díaz, B., Aster, Team, 2020. Timing of formation of neoglacial landforms in the South Shetland Islands (Antarctic Peninsula): regional and global implications. Quat. Sci. Rev. 234, 106248.
Piccini, C., Bertoglio, F., Sommaruga, R., Martínez de La Escalera, G., Pérez, L., Bugoni, L., Bergamino, L., Evangelista, H., García-Rodriguez, F., 2024. Prokaryotic richness and diversity increased during Holocene glacier retreat and onset of an Antarctic Lake. Commun. Earth Environ. 5, 94.
Pielou, E.C., 1966. The measurement of diversity in different types of biological collections. J. Theor. Biol. 13, 131–144.
Písková, A., Roman, M., Bulínová, M., Pokorný, M., Sanderson, D., Cresswell, A., Lirio, J. M., Coria, S.H., Nedbalová, L., Lami, A., Musazzi, S., Van de Vijver, B., Nývlt, D., Kopalová, K., 2019. Late-Holocene palaeoenvironmental changes at Lake Esmeralda (Vega Island, Antarctic Peninsula) based on a multi-proxy analysis of laminated lake sediment. Holocene 29, 1155–1175.
Priddle, J., Heywood, R.B., 1980. Evolution of Antarctic lake ecosystems. Biol. J. Linn. Soc. 14, 51–66.
Pudsey, C.J., Evans, J., 2001. First survey of Antarctic sub-ice shelf sediments reveals Mid-Holocene ice shelf retreat. Geology 29, 787–790.
Quayle, W.C., Convey, P., Peck, L.S., Ellis-Evans, C.J., Butler, H.G., Peat, H.J., 2003. Ecological responses of maritime Antarctic lakes to regional climate change. Antarct. Res. 79, 159–170.
Quayle, W.C., Peck, L.S., Peat, H., Ellis-Evans, J.C., Harrigan, P.R., 2002. Extreme responses to climate change in Antarctic lakes. Science 295, 645.
R Core Team, 2022. R: a Language and Environment for Statistical Computing. R Foundation for Statistical Computing, Vienna, Austria. https://www.R-project.org/.
Rabassa, J., 1983. Stratigraphy of the glacigenic deposits in northern James Ross Island, Antarctic Peninsula. In: Evenson, E., Schlüchter, C., Rabassa, J. (Eds.), Tills and Related Deposits. A. A. Balkema Publishers, Rotterdam, pp. 329–340.
Rabassa, J., Skvarca, P., Bertani, L., Mazzoni, E., 1982. Glacier inventory of James Ross and Vega Islands, Antarctic Peninsula. Ann. Glaciol. 3, 260–264.
Roberts, S.J., Hodgson, D.A., Sterken, M., Whitehouse, P.L., Verleyen, E., Vyverman, W., Sabbe, K., Balbo, A., Bentley, M.J., Moreton, S.G., 2011. Geological constraints on glacio-isostatic adjustment models of relative sea-level change during deglaciation of Prince Gustav Channel, Antarctic Peninsula. Quat. Sci. Rev. 30, 3603–3617.
Roberts, S.J., Monien, P., Foster, L.C., Loftfield, J., Hocking, E.P., Schnetger, B., Pearson, E.J., Juggins, S., Fretwell, P., Ireland, L., Ochyra, R., Haworth, A.R., Allen, C.S., Moreton, S.G., Davies, S.J., Brumsack, H.-J., Bentley, M.J., Hodgson, D. A., 2017. Past penguin colony responses to explosive volcanism on the Antarctic Peninsula. Nat. Commun. 8, 14914.
Robinson, S.A., Wasley, J., Tobin, A.K., 2003. Living on the edge – plants and global change in continental and maritime Antarctica. Global Change Biol. 9, 1681–1717.
Rochera, C., Camacho, A., 2019. Limnology and aquatic microbial ecology of Byers Peninsula: a main freshwater biodiversity hotspot in Maritime Antarctica. Diversity 11. https://doi.org/10.3390/d11100201.
Rouillard, A., Michelutti, N., Rosén, P., Douglas, M.S.V., Smol, J.P., 2012. Using paleolimnology to track Holocene climate fluctuations and aquatic ontogeny in poorly buffered High Arctic lakes. Palaeogeogr. Palaeoclimatol. Palaeoecol. 321–322, 1–15.
Roman, M., Chattová, B., Lehejček, J., Tejnecký, V., Vondrák, D., Luláková, P., Němeček, K., Houška, J., Drábek, O., Nývlt, D., 2021. Shallow depositional basins as potential archives of palaeoenvironmental changes in southwestern Greenland over the last 800 years. Boreas 50, 262–278.
Roman, M., Nedbalová, L., Kohler, T.J., Lirio, J.M., Coria, S.H., Kopáček, J., Vignoni, P. A., Kopalová, K., Lecomte, K.L., Elster, J., Nývlt, D., 2019. Lacustrine systems of Clearwater Mesa (James Ross Island, north-eastern Antarctic Peninsula): geomorphological setting and limnological characterization. Antarct. Sci. 31, 169–188.
Rydberg, J., Lindborg, T., Sohlenius, G., Reuss, N., Olsen, J., Laudon, H., 2016. The importance of eolian input on lake-sediment geochemical composition in the dry proglacial landscape of western Greenland. Arctic, Antarctic, and Alpine Research 48, 93–109.
Sanderson, D.C.W., 1988. Thick source beta counting (TSBC): a rapid method for measuring beta dose-rates. Nucl. Tracks Radiat. Meas. 14, 203–207.
Sanderson, D.C.W., Cresswell, A.J., Roman, M., Písková, A., Kopalová, K., Nývlt, D., Lirio, J.M., 2017. Luminescence profile measurements of sediment cores from Lake Esmeralda and Monolith Lake, James Ross Island Archipelago. In: SUERC Report, East Kilbride. University of Glasgow, Glasgow, p. 51.
Sanderson, D.C.W., Murphy, S., 2010. Using simple portable OSL measurements and laboratory characterisation to help understand complex and heterogeneous sediment sequences for luminescence dating. Quat. Geochronol. 5, 299–305.
Shannon, C.E., Weaver, W., 1949. The Mathematical Theory of Communication. Urbana University Press, Illinois, p. 117.
Simms, A.R., Bentley, M.J., Simkins, L.M., Zurbuchen, J., Reynolds, L.C., DeWitt, R., Thomas, E.R., 2021. Evidence for a "Little Ice Age" glacial advance within the Antarctic Peninsula – examples from glacially-overrun raised beaches. Quat. Sci. Rev. 271, 107195.
Skvarca, P., De Angelis, H., Ermolin, E., 2004. Mass balance of "Glaciar Bahía del Diablo". Vega Island, Antarctic Peninsula. Ann. Glaciol. 39, 209–213.
Smellie, J.L., 2021. Bransfield Strait and James Ross Island: Volcanology. In: Smellie, J. L., Panter, K.S., Geyer, A. (Eds.). In: Volcanism in Antarctica: 200 Million Years of Subduction, Rifting and Continental Break-up, 55. Geol. Soc, London, Mem, pp. 227–284.
Smellie, J.L., Johnson, J.S., McIntosh, W.C., Esser, R., Gudmundsson, M.T., Hambrey, M. J., van Wyk de Vries, B., 2008. Six million years of glacial history recorded in the James Ross Island Volcanic Group, Antarctic Peninsula. Palaeogeogr. Palaeoclim., Palaeoecol. 260, 122–148.
Smellie, J.L., Johnson, J.S., Nelson, A.E., 2013. Geological map of James Ross Island. I. James Ross Island Volcanic Group (1:125 000 scale). In: BAS GEOMAP 2 Series, Sheet 5. British Antarctic Survey, Cambridge, UK.
Sterken, M., Roberts, S.J., Hodgson, D.A., Vyverman, W., Balbo, A.L., Sabbe, K., Moreton, S.G., Verleyen, E., 2012. Holocene glacial and climate history of Prince Gustav Channel, northeastern Antarctic Peninsula. Quat. Sci. Rev. 31, 93–111.
Strunk, A., Olsen, J., Sanei, H., Rudra, A., Larsen, N.K., 2020. Improving the reliability of bulk sediment radiocarbon dating. Quat. Sci. Rev. 242, 106442.
Szeroczyfiska, K., Sarmaja-Korjonen, K., 2007. Atlas of subfossil Cladocera from central and northern Europe. Friends Low. Vistula Soc. Świecie 84.
Terauds, A., Lee, J.R., 2016. Antarctic biogeography revisited: updating the Antarctic Conservation Biogeographic Regions. Divers. Distrib. 22, 836–840.
Theilen, B.M., Simms, A.R., DeWitt, R., Zurbuchen, J., Garcia, C., Gernant, C., 2023. The impact of the Neoglacial and other environmental changes on the raised beaches of Joinville Island, Antarctica. Antarct. Sci. 35, 418–437.
Toro, M., Granados, I., Pla, S., Giralt, S., Antoniades, D., Galán, L., Cortizas, A.M., Lim, H. S., Appleby, P.G., 2013. Chronostratigraphy of the sedimentary record of Limnopolar Lake, Byers Peninsula, Livingston Island, Antarctica. Antarct. Sci. 25, 198–212.
Totten, R.L., Fonseca, A.N.R., Wellner, J.S., Munoz, Y.P., Anderson, J.B., Tobin, T.S., Lehrmann, A.A., 2022. Oceanographic and climatic influences on Trooz Glacier, Antarctica during the Holocene. Quat. Sci. Rev. 276, 107279.
Turner, J., Lu, H., White, I., King, J.C., Phillips, T., Hosking, J.S., Bracegirdle, T.J., Marshall, G.J., Mulvaney, R., Deb, P., 2016. Absence of 21st century warming on Antarctic Peninsula consistent with natural variability. Nature 535, 411–415.
Turner, J., Marshall, G.J., Clem, K., Colwell, S., Phillips, T., Lu, H., 2020. Antarctic temperature variability and change from station data. Int. J. Climatol. 40, 2986–3007.
Van de Vijver, B., Morales, E.A., Kopalová, K., 2014. Three new araphid diatoms (Bacillariophyta) from the Maritime Antarctic Region. Phytotaxa 167, 256–266.
van der Bilt, W.G.M., D'Andrea, W.J., Oppedal, L.T., Bakke, J., Bjune, A.E., Zwier, M., 2022. Stable Southern Hemisphere westerly winds throughout the Holocene until intensification in the last two millennia. Commun. Earth Environ. 3, 186.
van der Werff, A., 1955. A new method for cleaning and concentrating diatoms and other organisms. Verhandlungen Int. Ver. Für theoretische Angew. Limnol. 12, 276–277.
van Lipzig, N.P.M., King, J.C., Lachlan-Cope, T.A., van den Broeke, M.R., 2004. Precipitation, sublimation, and snow drift in the Antarctic Peninsula region from a regional atmospheric model. J. Geophys. Res. Atmos. 109, 1–16.
van Wessem, J.M., Reijmer, C.H., van de Berg, W.J., van den Broeke, M.R., Cook, A.J., van Ulft, L.H., van Meijgaard, E., 2015. Temperature and wind climate of the Antarctic Peninsula as simulated by a high-resolution regional atmospheric climate model. J. Clim. 28, 7306–7326.
Vaughan, D.G., Connolley, W.M., Parkinson, C., Mulvaney, R., Hodgson, D.A., King, J.C., Pudsey, C.J., Turner, J., 2003. Recent rapid regional climate warming on the Antarctic Peninsula. Clim. Change 60, 243–274.
Verleyen, E., Hodgson, D.A., Sabbe, K., Vyverman, W., 2004. Late Quaternary deglaciation and climate history of the Larsemann Hills (East Antarctica). J. Quat. Sci. 19, 361–375.
Verleyen, E., Van de Vijver, B., Tytgat, B., Pinseel, E., Hodgson, D.A., Kopalová, K., Chown, S.L., Van Ranst, E., Imura, S., Kudoh, S., Van Nieuwenhuyze, W., Consortium ANTDIAT, Sabbe, K., Vyverman, W., 2021. Diatoms define a novel freshwater biogeography of the Antarctic. Ecography 44, 548–560.
Vorrath, M.E., Müller, J., Cárdenas, P., Opel, T., Mieruch, S., Esper, O., Lembke-Jene, L., Etourneau, J., Vieth-Hillebrand, A., Lahajnar, N., Lange, C.B., Leventer, A., Evangelinos, D., Escutia, C., Mollenhauer, G., 2023. Deglacial and Holocene sea-ice and climate dynamics in the Bransfield Strait, northern Antarctic Peninsula. Clim. Past 19, 1061–1079.
Webster, J., Hawes, I., Downes, M., Timperley, M., Howard-Williams, C., 1996. Evidence for regional climate change in the recent evolution of a high latitude pro-glacial lake. Antarct. Sci. 8, 49–59.
Wei, T., Simko, V., 2016. R package 'corrplot': visualization of a correlation matrix, Version 0.80. Available from: https://github.com/taiyun/corrplot.
Wintle, A., Murray, A., 2000. Quartz OSL: effects of thermal treatment and their relevance to laboratory dating procedures. Radiat. Meas. 32, 387–400.
Zale, R., Karlén, W., 1989. Lake sediment cores from the Antarctic Peninsula and surrounding islands. Geogr. Ann. Ser. A 71, 211–220.
Zidarova, R., Kopalová, K., Van de Vijver, B., 2016. Diatoms from the Antarctic Region. I: Maritime Antarctica. In: Lange-Bertalot, H. (Ed.):. In: Iconographia Diatomologica, vol. 24. Koeltz Botanical Books, 509 pp.